Numerical investigation of spreading time in droplet impact with spherical surfaces: from physical analysis to data-driven prediction model

Ikroh Yoon, Seungwon Shin, Damir Juric, Jalel Chergui

Numerical investigation of spreading time in droplet impact with spherical surfaces: from physical analysis to data-driven prediction model

Ikroh Yoon[1,a], Seungwon Shin[2], Damir Juric[3,4] and Jalel Chergui[3]

[1] Korea Institute of Marine Science and Technology Promotion (KIMST), 06775 Seoul, Korea (currently works at Intergovernmental Oceanographic Commission of United Nations Educational, Scientific and Cultural Organization, 75007 Paris, France), iryoon@kimst.re.kr

[2] Department of Mechanical and System Design Engineering, Hongik University, 04066 Seoul, Korea, sshin@hongik.ac.kr

[3] Centre National de la Recherche Scientifique (CNRS), Laboratoire Interdisciplinaire des Sciences du Numérique (LISN), Université Paris Saclay, 91400 Orsay, France, Damir.Juric@lisn.fr, Jalel.Chergui@lisn.fr

[4] Department of Applied Mathematics and Theoretical Physics, University of Cambridge, Centre for Mathematical Sciences, Wilberforce Road, Cambridge CB3 0WA, UK

[a)] Corresponding Author:
Senior researcher, Ikroh Yoon, PhD
E-Mail: iryoon@kimst.re.kr

ABSTRACT

Spreading time, the time that an impacting droplet attains the maximum wetting area on a solid surface, plays a critical role in many engineering applications particularly where heat transfer or chemical reactions are involved. Although the impact dynamics of a droplet significantly differ across the different spreading regimes depending on various collision parameters, it still remains unclear (i) how the spreading time changes for each spreading regime, and (ii) how the target curvature can affect the spreading time. In the present study, the spreading time during droplet impact on a spherical target is systematically studied at the three different spreading regimes for a wide range of impact parameters (Weber number, equilibrium contact angle, Ohnesorge number and droplet-to-target size ratio). The changes of spreading time depending on the impact parameters and underlying physical mechanisms are analyzed in detail at the level of three different spreading regimes. Our results show that the spreading time, proper time scales, dominant impact parameters and associated physical behaviors all significantly and non-linearly change across the three spreading regimes. An improved prediction model for the spreading time is also proposed for each regime, which is now based on only the controllable variables and has an explicit form. The effect of target curvature on the spreading time is further investigated, and finally, a data-driven prediction model is proposed to represent the complicated and non-linear nature of the spreading time broadly across the three spreading regimes.

Keywords: droplet impact; spreading time; multiphase flow simulation; prediction model; data-driven analysis

I. INTRODUCTION

Collisions of droplets with solid surfaces can be found not only in a broad range of modern technologies but also in everyday life [1,2]. Since droplet collision phenomena can play crucial roles in the performance of diverse engineering applications such as spray cooling and chilling [3], spray drying [4], wet-scrubbers [5], fluid catalytic cracking (FCC) [6], trickle-bed reactors [7], microfluidic-based encapsulation of biomaterials [8] and tablet coating [9], to name a few examples, their collision processes have naturally been of great interest across various fields of chemical, mechanical, pharmaceutical, food and bio industries [1,9-11]. In general, the collision behavior is dominated by a complicated competition and interaction among inertial, viscous, and capillary forces (sometimes including the gravitational force as well) at very small length and time scales [12,13].

For droplet impact problems with a solid surface much effort has focused on investigating the maximum spreading extent (normally characterized by the maximum spreading diameter) [14-17] and the spreading time [18-21]. The former measures "how much a droplet can spread over a target surface", while the latter quantifies "how long it takes to reach the maximum spreading state". Both quantities usually play critical roles in determining process performance and efficiency particularly in the context of controlling the droplet deposition process [1,12,19]. For example, the maximum spreading extent of a catalyst particle significantly affects the catalyst efficiency as well as the system performance of trickle-bed reactors [7] and the spreading time also plays an important role in collision processes where heat transfer (e.g., droplet solidification) [14] and/or chemical reactions (e.g., cracking reaction in the FCC system) [22] are involved.

After Chandra and Avedisian's work [23] which has initiated a series of energy-balance-

based theoretical approaches for estimating the maximum spreading diameter of droplets numerous studies have been devoted to the spreading dynamics of droplets on a solid surface. Based on the concept of the energy-balance between the collision instant and the maximum spreading state Pasandideh-Fard *et al*. [24] proposed more refined length and time scales to evaluate the energy loss in the boundary layer where the viscous dissipation occurs and their approach has indeed provided a cornerstone for many later theoretical energy-balance-based approaches [25,26]. This type of analysis was also widely utilized for estimating the rebound criteria of bouncing droplets on a non-wettable surface [25] as well as the maximum spreading extent [23-26]. Afterward, Roisman [27] considered the full Navier-Stokes equations to estimate the flow field inside the droplet and proposed a semi-empirical model using the experimentally fitted data. Later, his model was experimentally demonstrated to be one of the most accurate models for the maximum spreading extent for a wide range of Weber number and surface wettability [14]. Wilderman *et al*. [17] presented an interesting analysis for high-speed drop impact problems. They showed that roughly one-half of the initial (impact) kinetic energy can be converted into surface energy owing to a universal head loss regardless of detailed impact conditions and energy dissipation mechanisms. More recently some other sources causing extra energy loss during the spreading stage of droplets have been found to affect the maximal spreading extent, e.g., residual kinetic energy in the form of vortical flow inside a droplet [16] or energy loss due to 'interface relaxation' near a solid surface [18]. Although there is still a debate on the maximum spreading extent [28], in general, scaling laws of $We^{1/4}$ derived from momentum conservation [16] and $We^{1/2}$ derived from energy conservation [29] have been experimentally shown to hold for the inviscid regime (for less viscous droplets) whereas a $Re^{1/5}$ rule [30] has worked well for a viscous regime (for highly viscous droplets).

There have also been several attempts to examine spreading dynamics for droplet

collision on curved surfaces such as a spherical target. Bakshi *et al*. [31] experimentally showed that the film thickness at the collision center undergoes three different phases: (i) initial drop-deformation, (ii) inertia-dominated and (iii) viscosity-dominated. The dimensionless film thickness profiles were collapsed on a single curve for the first and second phases. Malgarinos *et al*. [32] used volume-of-fluid (VOF) simulation to study the problem of drop collision on spherical targets. They investigated the boundary separating the coating from the rebound regime, the film thickness, and the wetted area. Afterward, they further performed extensive VOF simulations to study drop impact on a spherical particle including phase change and reaction phenomena in a high temperature environment ($T \geq 800$ K) [33]. Zhang *et al*. presented two-dimensional [34] and three-dimensional [35] Lattice-Boltzmann simulations. They examined the effects of Weber and Reynolds numbers on the film thickness at the collision center, and their simulation results reproduced Bakshi *et al*.'s [31] experimental observations well. Liang *et al*. [36] experimentally studied drops impacting on wetted spherical targets, and they showed the drop-to-target curvature ratio played a critical role in not only the spreading characteristics but also determining the splashing threshold. Mitra *et al*. [37], Liu *et al*., [38], and Khurana *et al*. [39] proposed energy-balance-based prediction models for evaluating the spreading extent on a spherical surface and their models reproduced their experimental observations well. Yoon and Shin [40] also proposed scaling laws and an empirical correlation for the maximum spreading diameter of a droplet colliding with a spherical surface for a wide range of liquid viscosity. More recently, Yoon *et al*. [41] proposed a data-driven prediction model for the maximum spreading that can be applied to both a flat surface and a spherical surface. Although these studies reviewed above have provided useful relations to estimate the maximum spreading extent as well as have notably shed light on our understanding of the physical mechanisms of spreading droplets, they have mainly focused on the maximum spreading extent itself rather than on the spreading time.

We now review studies in the context of the spreading time which has been relatively less well-explored compared to the maximum spreading extent. Although it has long been understood that the contact time of a droplet is limited by the Rayleigh oscillation time [42] which is a function of the drop's density, diameter and surface tension coefficient, the energy-balance-based approaches, at the very early stage, simply approximated the spreading time τ ignoring the effect of surface tension. Chandra and Avedisian [23] considered τ to be $\tau = D_d / V_{ini}$, where D_d and V_{ini} are the initial droplet diameter and the impact velocity, respectively. This is indeed the advective characteristic time scale which has normally been used to nondimensionalize the physical time scale [31], and also can be interpreted as the required time for a droplet to reach zero height from its initial diameter, D_d, at a constant impact velocity V_{ini}. Pasandideh-Fard *et al*. [24] modified the spreading time to be $\tau = 8D_d / 3V_{ini}$ based on a simple geometric assumption and mass conservation and their model has been widely used in many other theoretical studies [26,43]. Recently, Antonini and Amirfazli [14] experimentally showed that the spreading time τ is considerably affected by surface wettability. Lee *et al*. [44] also presented significant effects of liquid properties on τ. They replaced the initial drop diameter (D_d) in Pasandideh-Fard *et al*.'s model [24] with D_m (where D_m is the maximum spreading diameter), suggesting an empirical model, $\tau = b(D_m/V_{ini})$, where b is the ratio of the surface tension coefficient between a working droplet and a water droplet. Huang and Chen [18] and Wang *et al*. [45] also adopted a similar spreading time as the model of Lee *et al*. [44]. Lin *et al*. [19] presented a remarkable experimental study for the spreading time and systematically analyzed the effects of various collision parameters (e.g., impact velocity, liquid properties and surface wettability) on τ for a very wide range of collision conditions. They also proposed a new empirical model for the spreading time as a function of Weber number, i.e., $\tau^* = 0.92We^{-0.43}$. Here, τ^* is the rescaled spreading time using a modified capillary time scale $(\rho D_m^3/8\sigma)^{0.5}$ based on the maximal spreading diameter, D_m,

where ρ and σ are the density of a droplet and the surface tension coefficient, respectively. Du *et al*. [21] also proposed a similar empirical model ($\tau^* = 1.47We^{-0.44}$) as Lin *et al*.'s model [19]. More recently, Aksoy *et al*. [20] showed the effect of liquid viscosity on the spreading time and proposed an empirical model as a function of both Weber and Reynolds number, i.e., $\tau^* = 2We^{-0.45}Re^{-0.09}$.

Even considering the numerous studies heretofore undertaken, it still remains difficult to comprehensively understand how the spreading time of a droplet can be affected by various collision parameters for a wide range of impact parameters. In particular, one can find significant knowledge gaps as follows:

(i) It is well-known that drop spreading dynamics vary significantly across the different spreading regimes. For example, a drop's physical behavior and its maximum spreading extent change considerably across inviscid and viscous regimes [16,29,30]. However, it is still unclear how the spreading time (τ) changes for different spreading regimes, because the existing studies have usually studied the global behavior of spreading time at a general level, not focused on detailed changes and associated physical mechanisms at the level of each different spreading regime.

(ii) Although the significant effects from impact parameters (e.g., We, Re, surface wettability, etc.) on the spreading time have been evidently demonstrated by many experiments [14,18-20,44], it is not easy yet to model the spreading time using those impact parameters. All recent scaling laws (or empirical models) reviewed above [18-21,44,45] have still been a function of the maximum spreading diameter (D_m) which is usually unknown. Since the effects of impact

parameters are already reflected in D_m [14-17,25,27], D_m cannot be considered as a controllable independent variable to model τ resulting in the limitation of direct "physical interpretation" of relations between the impact parameters and the spreading time. In addition, the existing models [18-21,44,45] cannot be explicitly solved due to the multiple unknown variables (i.e., the maximum spreading diameter and the spreading time) leading to inconvenience for users.

(iii) The effect of surface curvature on the spreading time has not been systematically investigated so far. Although a few recent numerical studies [46,47] have demonstrated that the surface curvature can affect the spreading time of the droplet collision system, it is still unclear that how the spreading time changes depending on the surface curvature for different spreading regimes. In addition, to the best of our knowledge, there has not yet been a prediction model for the spreading time which can consider the effect of surface curvature.

In this study, we expand our previous work [41] which examined the maximum spreading extent, now focusing on the systematic investigation of the spreading time which is another important design parameter in the droplet collision system. Based on our verified computational framework, effects of important impact parameters (i.e., collision velocity, surface wettability, liquid viscosity, surface tension and surface curvature) on the spreading time are quantified for a wide range of impact parameters. In particular, detailed changes in the spreading time and associated underlying mechanisms are analyzed for three different spreading regimes to better understand the complicated physical behaviors. A new prediction model for the spreading time using only controllable independent variables is presented for each regime, and a data-driven prediction model for the entire spreading regime is also

proposed broadly covering all ranges of impact parameters considered in the present study.

The remainder of the current paper is organized as follows: Section II provides a brief introduction of the simulation methods used herein. Section III quantitatively and systematically examines the spreading time of a droplet collision system. Physical analysis and prediction models are also presented in this section. The major findings are summarized in Section IV.

II. COMPUTATIONAL FORMULATION

Since we primarily focus on understanding the physical characteristics of the spreading time, and have utilized the same computational framework as in our previous studies [40,41,48,49], we provide here a brief introduction of our numerical methods used in this study rather than a fully detailed explanation. For more algorithmic details and relevant techniques on our simulation methods, and for our various benchmark tests including grid convergence characteristics, readers can refer to our previous work [40,41,48,49]. Note also that our computational framework has been extensively applied to diverse droplet collision cases for various types of solid surface including flat substrates [49], spherical objects [40,41,48], cylindrical targets [50] and has also been streamlined (using an adaptive-mesh-refinement approach [51]) and parallelized [52].

For incompressible flows the governing equations can be applied to all three phases (solid, liquid and gas) and are solved on a fixed Cartesian (Eulerian) grid as a single-field formulation:

$$\nabla \cdot \mathbf{u} = 0 \tag{1}$$

$$\rho\left[\frac{\partial \mathbf{u}}{\partial t}+\mathbf{u}\cdot\nabla\mathbf{u}\right]=-\nabla P+\rho\mathbf{g}+\nabla\cdot\mu\left(\nabla\mathbf{u}+\nabla\mathbf{u}^{\mathrm{T}}\right)+\mathbf{F} \tag{2}$$

where $\mathbf{u}$, P and $\mathbf{g}$ are the velocity vector, the pressure, and the gravitational acceleration, respectively. ρ is the density and μ is the viscosity. The surface tension force $\mathbf{F}$ is considered only at the phase (gas-liquid) interface and can be modeled by the following hybrid representation based on the continuum-surface-force (CSF) formulation [53]:

$$\mathbf{F}=\sigma\kappa_{\mathrm{H}}\nabla I \tag{3}$$

where κ_{H} is the curvature field. Note that I is the indicator function which has the characteristics of the Heaviside function, varying from 0 (zero) in one phase (liquid droplet) to 1 (one) in the other phase (ambient air).

The physical properties of both phases (i.e., the ambient air and the liquid droplet) can also be assigned by using the indicator function I as follows:

$$\rho=\rho_{\mathrm{d}}+\left(\rho_{\mathrm{a}}-\rho_{\mathrm{d}}\right)I \tag{4}$$

$$\mu=\mu_{\mathrm{d}}+\left(\mu_{\mathrm{a}}-\mu_{\mathrm{d}}\right)I \tag{5}$$

Here, the subscript “d” denotes droplet, whereas “a” denotes air. Note that this common approach has been broadly applied to various multiphase-flow simulations and more detailed techniques dealing with the surface tension force and the physical properties near the gas-liquid phase interface can be found in Unverdi and Tryggvason [54] and Brackbill *et al.* [53].

Our dynamic contact angle modeling technique is given in Appendix A, and further details of the discretization of the governing equations, time-stepping, and other solution techniques used in the present study can also be found in Yoon *et al*. [41] and Yoon and Shin [48].

One of the most essential algorithms for this type of multiphase-flow simulation is an interface tracking method. Here we use the level contour reconstruction method (LCRM) [55-57] to track the gas-liquid phase interface. The LCRM is a hybrid method benefitting from two of the most well-established and popular interface tracking methods, i.e., level set [58] and front tracking [54]. In the LCRM the phase interface is basically represented by using (Lagrangian) moving marker elements (lines in 2D simulations and triangles in 3D simulations, as in the original front tracking method) but the moving elements are re-meshed using the distance function which is the key feature of the level set method. Such a reconstruction procedure can allow us to avoid the algorithmic complexity of dealing with the connectivity among the moving interface elements which is the most well-known shortcoming of the original front tracking method. Note that each moving element can always be implicitly (naturally) interconnected without any further artificial connection technique because the reconstruction procedure is performed at each boundary between cells (i.e., at cell faces) on the fixed Cartesian grid. Note also that the LCRM retains the tracking capability of the original front tracking method (i.e., accurate representation of the phase interface using moving markers) while avoiding the complex algorithmic difficulties in handling the topology changes (e.g., deformation, pinch-off or coalescence of the phase interface). For more details on the LCRM readers can refer to Shin and Juric [55,56].

Figure 1 illustrates the simulation geometry and boundary conditions used in this study. All simulations are performed in a (two-dimensional) axi-symmetric domain. The axi-symmetric boundary condition is set for the left boundary whereas open boundary conditions are set for the right, upper and lower boundaries. The lengths of the physical domain are set

as R_L = 7.5 (in the radial r direction) and Z_L = 20 (in the axial z direction) times the droplet radius, respectively, which are sufficiently large compared to the size of the droplet. Note that near the splashing threshold [59,60] the droplet rim may exhibit considerable asymmetric behavior along the circumferential direction (e.g., fingering or cusp of lamella [12,13]). Therefore, we set the simulation conditions sufficiently below the splashing threshold (specific conditions will be described later) to ensure that our axi-symmetric formulation can be a reasonable approach to reducing the necessary computational resources [41,51]. A droplet impacts onto a stationary spherical target at an initial impact velocity, (V_{ini}) and D_s is the diameter of the spherical target where the subscript "s" denotes the target surface.

III. RESULTS AND DISCUSSION

The spreading dynamics of a droplet on a solid surface is primarily dominated by a complicated time-and-space dependent interplay among inertial, viscous, and capillary effects [12,13] and to characterize their relative importance, three non-dimensional variables, i.e., the Weber number (We = $\rho_d V_{ini}^2 D_d/\sigma$), the Reynolds number (Re = $\rho_d V_{ini} D_d/\mu_d$) and the Ohnesorge number [Oh = $\mu_d/(\rho_d \sigma D_d)^{0.5}$] have usually been used. Because Oh can also be represented by using We and Re (i.e., Oh = $We^{0.5}$/Re) the spreading dynamics can basically be characterized by two of these numbers. Here we use We and Oh as impact parameters with two other variables, i.e., the equilibrium contact angle (θ_{eqi}) and the droplet-to-target size ratio (Ω) which characterize surface wettability and the curvature of the target surface, respectively.

Three characteristic time scales are considered, i.e., the advective time, $t_a = D_d/V_{ini}$ [30,61], the capillary time, $t_c = (\rho D_d^3/8\sigma)^{0.5}$ [16,62], and the viscous time. $t_v = \mu_d D_d/\sigma$ [16,62]. The physical time scale, t, can be non-dimensionalized by the three characteristic time scales

above and the non-dimensional advective, capillary, and viscous time scales are denoted by t_a^* ($t_a^* = t / t_a$), t_c^* ($t_c^* = t / t_c$), t_v^* ($t_v^* = t / t_v$), respectively.

To sufficiently cover the broad range of impact parameters, and to systematically examine the effects of impact parameters on the spreading time, we consider a total of 2400 collision cases. The droplet diameter and the density are fixed at D_d = 2 mm and ρ_d = 998.2 kg/m^3, respectively. The physical properties of the gas phase (ambient air) and the surface tension coefficient are also fixed (ρ_a = 1.2 kg/m^3, μ_a = 0.000018 N s/m^2, and σ = 0.0728 N/m).

Four collision parameters, i.e., We, Oh, θ_{eqi} and Ω are varied by controlling the impact velocity (V_{ini}), droplet viscosity (μ_d), equilibrium contact angle (θ_{eqi}) and the diameter of the target (D_s), respectively. The splashing threshold is usually described by We and Oh [59,63], and splashing can be observed more easily on a small spherical target compared to that on a flat substrate [63]. Since splashing can occur near We ~ 150 – 160 if Ω ~ 1/4 – 1/2 (for millimetric water drops, Oh ~ 0.0026) [48,63], we consider a range of Weber number below 110 ($1 \leq We \leq 110$) to ensure that the collision outcomes would not fall into the splashing region. Therefore, a total of 12 cases of We (i.e., We = 1, 2, 4, 6, 8, 10, 20, 30, 50, 70, 90, and 110) are selected (the initial impact velocity V_{ini} is varied from 0.190 to 2.003 m/s).

Also, we considered a broad range of Oh number ($0.0013 \leq Oh \leq 0.7869$), a total of 10 cases of Oh (i.e., Oh = 0.0013, 0.0026, 0.0052, 0.0104, 0.0262, 0.0525, 0.1049, 0.2620, 0.5246 and 0.7869) are selected (the droplet viscosity μ_d is varied from 0.0005 to 0.3 N s/m^2). Note that such a range of droplet viscosity considered herein corresponds to a range of 0.5 – 300 times the viscosity of a water droplet which covers a range of Oh of most practical interest among diverse engineering fields, e.g., gasoline (Oh ~ 0.0018), water (Oh ~ 0.0026), ethyl alcohol (Oh ~ 0.0063), squalene (Oh ~ 0.05), and printable ink (Oh ~ 0.1–1.0) with the given droplet diameter (2 mm) [64,65]. 5 cases of θ_{eqi} (i.e., θ_{eqi} = 20°, 55°, 90°, 125° and 160°) are also selected to cover a wide range of surface wettability from hydrophilic to

(super) hydrophobic surfaces.

The impact physics on a spherical target is practically identical to that on a flat substrate if a droplet collides onto a sufficiently large spherical target which has a diameter 10 times larger than the droplet (i.e., $\Omega \leq 1/10$) [38,47]. Note that this assumption has been experimentally [38] and numerically [40,41] confirmed. Conversely, collision dynamics can differ greatly on a sufficiently small spherical target because a target can be fully coated by the droplet. In this case the typical maximum spreading state cannot be observed and full coating can usually be observed where $\Omega \geq 1/1.5$ [39,48]. Therefore, we here examine the effect of target size between those two thresholds ($1/10 \leq \Omega \leq 1/1.5$) and 4 cases of the droplet-to-target size ratio (i.e., $\Omega = 1/10, 1/4, 1/3, 1/2$) are selected.

As a result, a total of 2400 collision cases (12 Weber numbers, 10 Ohnesorge numbers, 5 surface wettabilities and 4 droplet-to-target size ratios) are considered in the current study. This large dataset will also be used to train a deep neural network to formulate a data-driven prediction model as a non-linear regressor as well as to systematically examine the effects of 4 collision parameters (We, Oh, θ_{eqi} and Ω) on the physical behavior of the spreading time. For more details of the simulation settings readers can also refer to our previous study [40,41].

A. Review of typical spreading dynamics

The schematic diagram in Figure 2 summarizes the different spreading regimes for the droplet-solid collision system depending on its physical behavior. If a droplet collides onto a solid surface with sufficiently high inertia, splashing can occur where tiny re-atomized droplets are generated [12,13]. It has been found that higher We and lower Oh normally promote splashing [59] but the detailed threshold for the onset of splashing can also be affected by many other collision environments, e.g., surface roughness [63], target curvature

[63] and ambient gas pressure [60], etc. Conversely, if a droplet impacts onto a solid surface with very low inertia compared to surface tension, i.e., at very low Weber number (We ≤ 1), a droplet can behave like an elastic ball, sometimes bouncing off a solid surface numerous times [66]. This region is the so-called elastic regime.

Between those two thresholds (i.e., above the elastic threshold and under the splashing threshold), in general, a droplet spreads over a solid surface and then reaches a maximum spreading state. Afterward, the droplet can retract and is eventually deposited on a surface (or can also bounce off a surface depending on surface hydrophobicity) [12,13]. Such a spreading regime can typically be categorized into the following three sub-regimes depending on the underlying physical mechanisms: (i) capillary-driven spreading at relatively low Weber number [41,61], (ii) inertia-driven but capillary-limited (inviscid) at high We and low Oh [16,40,62] and (iii) inertia-driven but viscous-limited at high We and high Oh [16,40,62].

If We is sufficiently small (i.e., We on the order of 10^0), spreading dynamics is primarily driven by capillary effects acting on the three-phase triple contact line [61,67,68]. At such a capillary-driven spreading regime (i.e., regime 1 in Fig.2, also denoted as "CD regime" hereafter), surface wettability and the associated wetting nature can play more significant roles in the spreading process rather than inertial effects due to the low Weber number [18,41]. At a very early stage of contact the apparent contact angle (θ_{ap}) is nearly 180° which is far from its equilibrium contact angle (θ_{eqi}). Therefore, the capillary force which can be scaled as $F_c \sim \sigma R_w(\theta_{ap} - \theta_{eqi})$ (where R_w is the contact radius) starts to act near the contact line and drive the spreading process. Note that this capillary effect can make a droplet spread over a solid surface even if the initial collision velocity is zero and it has also been experimentally [15] and numerically [41] confirmed that the maximum spreading extent of millimetric droplets can be larger than the initial droplet diameter in cases of zero impact velocity. In Fig.2 the CD regime is indicated by the blue region.

If We is sufficiently large [i.e., We ≥ $O(10^1)$] but Oh is small [i.e., Oh ≤ $O(10^{-2})$], the spreading process is primarily governed by inertial effects but is terminated by the capillary limit [16,40,62]. At this inertia-driven but capillary-limited (inviscid) regime (i.e., regime 2 in Fig.2, also denoted as "IC regime" hereafter), the effects of surface wettability and viscous dissipation play minor roles in the spreading process, due to the high We and low Oh numbers. In other words, a droplet can spread over a surface until the interfacial deformation is no longer available. The spreading dynamics in the IC regime can also be characterized by the ejection of a thin liquid sheet (i.e., jetting lamella) at the initial stage [69], and considerable deformation of the leading edge outer rim can be expected during the subsequent spreading stage [27,40,70]. The maximum spreading extent can be scaled by the Weber number, and $We^{1/4}$ [16,40,62] and $We^{1/2}$ [29] rules have been shown to work well. In Fig.2 the IC regime is indicated by the red region.

On the other hand, if both We and Oh are sufficiently large [i.e., We ≥ $O(10^1)$ and Oh ≥ $O(10^{-2})$], the spreading process is primarily governed by inertial effects but is terminated by the viscous limit [16,40,62]. At this inertia-driven but viscous-limited spreading regime (i.e., regime 3 in Fig.2, also denoted as "IV regime" hereafter), the effect of viscous dissipation plays a significant role whereas the effect of surface wettability is still negligible due to the high We and Oh numbers. In other words, a droplet can spread over a surface until all the initial impact (kinetic) energy is dissipated by viscous damping. No lamella ejection is expected in this viscous regime [19] owing to the strong viscous resistance which hinders the interfacial deformation. The maximum spreading extent can be scaled by the Reynolds number and a $Re^{1/5}$ rule has been found to hold well [16,29,40,62]. In Fig.2 the IV regime is indicated by the green region.

Note that, in the present study, we focus on these three spreading regimes (i.e., CD, IC, and IV regimes). The other collision regimes (elastic regime and splashing regime) are

beyond the current scope due to their different collision phenomena and different area of interest among the scientific communities.

Figure 3 depicts the typical spreading processes of droplets for the three different spreading regimes summarized in Fig.2 above. The morphological evolutions of spreading droplets for the CD, IC, and IV regimes are presented in Fig.3(a), (b), and (c), respectively. Note that the (non-dimensional) advective time scale (t_a^*) is used for all cases in Fig.3, since here we simply focus on describing the typical spreading processes rather than addressing their detailed physical interpretations. Note also that the collision cases where Ω = 1/10 which can reasonably be regarded as a flat substrate [38,47] are considered in Fig.3 due to its generality. As seen in Fig.3(a), the capillary effect acting near the contact line drives the spreading process for the CD regime. The upper-part of the droplet can nearly maintain its spherical shape owing to the low Weber number (low impact velocity), whereas a capillary wave is formed above the contact line due to the local interfacial curvature [see t_a^* = 0.34 in Fig.3(a)] [18,19,68]. As the capillary waves propagate to the central part of the droplet, the droplet shows a staircase-like pyramidal structure [18,19,68] without significant interface deformation ($0.34 \leq t_a^* \leq 0.50$). After the maximum spreading state, the oscillatory motion of the central part is observed in the vertical direction and then the droplet reaches an equilibrium state ($0.50 \leq t_a^* \leq 5.00$).

In the IC regime, as seen in Fig.3(b), a thin liquid sheet (lamella) is ejected above the solid surface due to the strong inertial effect overwhelming the surface tension without significant viscous resistance [see t_a^* = 0.25 in Fig.3(b)]. The droplet rapidly spreads over the surface and the thin lamella continues consuming liquid mass, forming a thick rim at the leading edge of the lamella ($0.80 \leq t_a^* \leq 1.74$) [27,40,61,70]. As the lamella spreads on a surface, the leading edge of the lamella is detached from the surface due to its strong radial motion at t_a^* = 0.80. After the maximum spreading state, the droplet starts its retraction

motion, driven by the capillary effect, to reduce the increased surface energy during the spreading stage ($1.74 \leq t_a^* \leq 8.00$).

In the IV regime, as explained above, no notable lamella ejection is observed [19]. The interfacial deformation is significantly hindered by the strong viscous damping. After the maximum spreading state ($t_a^* = 0.98$), the central part of the droplet slightly and slowly rises again, reaching the equilibrium state, but no meaningful recoiling motion is seen in terms of its wetted area. Note that all these results showing the evolutions of the droplet morphologies for the three spreading regimes depicted in Fig.3 are consistent with the experimental observations of Lin *et al*. [19].

Figure 4 quantifies the temporal evolution of the spreading extent characterized by the non-dimensional spreading diameter β^* ($\beta^* = \beta/D_d$ where β denotes the arc length of the droplet in contact with a solid target, see the inset in Fig.4) of the droplets for the three collision cases shown in Fig.3. Note that, for the CD and the IC regimes, detecting the spreading time with the maximum value of β^* can be straightforward because the droplet starts its recoiling motion soon after the maximum spreading state (see black solid line and blue dashed line). The corresponding time for the maximum value of β^* is visually evident. Conversely, as shown in Fig.3(c), usually no obvious recoiling stage occurs for the IV regime due to the high viscous resistance (see red dotted line in Fig.4). In this case, detecting the spreading time can be quite confusing and even a very small disturbance in β^* can lead to a critical bias for measuring the spreading time. Therefore, to avoid such a complexity, the time when a droplet attains 95 % of the maximum value of β^* is defined as the spreading time as marked by three triangles in Fig.4 (see also green arrow). Note that, hereafter, the non-dimensional forms of the spreading time are denoted by τ_a (if the advective time scale is used), τ_c (if the capillary time scale is used) and τ_v (if the viscous time scale is used).

B. Validations

In the above subsection, we addressed the typical spreading dynamics for the three different spreading regimes. Before we start analyzing the spreading time for each regime in more detail in this subsection, we validate our simulation method by comparisons with existing experimental results to check its capability for simulating the droplet collision phenomena in terms of the spreading time.

Figure 5 compares our simulation results with the experimental data of Mitra *et al*. [2] and Banitabaei and Amirfazli [71] focusing on the collision behavior on spherical targets for a broad range of We (We = 0.9 – 155.5). First, Fig.5(a) depicts the temporal variation of β^* and the morphological evolution of the droplet for the low Weber number case (We = 0.9). The insets in Fig.5(a) shows the interfacial shapes captured by the experiment (on the right side of each panel) [2] and by the current simulation (on the left side of each panel) at three different time instants (t_a^* = 0.24, 0.47, and 0.71). As seen, our simulation result shows a good agreement with the experimental observation. Fig.5(b) depicts the temporal variation of the non-dimensional film thickness, h^* [$h^* = h/D_d$, where h is the liquid film thickness measured on the impact center, see the inset on the lower-left corner in Fig.5(b)] and the morphological evolutions of the droplet for the high Weber number case (We = 155.5). The other insets in Fig.5(b) show the interfacial shapes captured by the experiment [71] and by the current simulation at four different time instants (t_a^* = 0.30, 0.60, 1.05 and 1.95). Again, our simulation result shows a good agreement with the experimental observation. Since the liquid film thickness is one of the most sensitive parameters to the mesh size in this type of numerical simulations [72], we here present our grid-convergence test result as well in Fig.5(b). As seen in the dashed gray box, our simulated h^* almost converges at 32 CPR (cells per radius) as in our previous study [48,51]. Overall, our simulation result shows an excellent agreement with the experimental result [71] in terms of both qualitative and quantitative

469 comparisons. Note also that all simulation cases presented in the current study have been
470 performed with 64 CPR to be on the safe side.

471 In figure 6 we further validate our simulation results focusing on the quantification of the
472 spreading time for a broad range of We and Oh. Fig.6(a) depicts the non-dimensional
473 spreading time, τ_a, for the low Oh case (Oh = 0.0026 for a water drop). As seen, our
474 simulation result is consistent with the experimentally measured data of Huang and Chen
475 [18]. A small deviation can be attributed to the difference of the definition of spreading time
476 (i.e., we defined the spreading time as the time that a droplet attains 95% of the maximum
477 spreading extent. See Fig.4 and its explanation). In Fig.6(b), we compare the simulated τ_a
478 with the existing numerical result [21] and empirical correlation [19] for the high Oh case
479 (Oh = 0.62 in the case where the droplet is 240 times the viscosity of a water drop). Our
480 result again shows an excellent agreement with the existing results [19,21].

481 Further validation test results for drop impact problems are also extensively provided in
482 Appendix B, which were presented in our previous study. From Figs.5 – 6 and Appendix B,
483 we can conclude that our simulation methods used in this study can reasonably reproduce the
484 experimental data for a wide range of collision parameters in the context of both qualitative
485 and quantitative comparisons. Note that the current numerical framework has been widely
486 applied to various droplet-solid collision problems and has been thoroughly validated against
487 many existing experimental data [40,41,48,49,51]. Note also that the impact parameters
488 considered in our current and previous validation tests reasonably cover the practical
489 conditions used in the current study ($0 \leq We \leq 110$, $20° \leq \theta_{eqi} \leq 160°$, $0.0013 \leq Oh \leq 0.7869$
490 and $1/10 \leq \Omega \leq 1/2$).

491

492 **C. Effects of collision parameters on the spreading time and prediction**
493 **models**

We now analyze the spreading time for the three different spreading regimes addressed above, i.e., the capillary-driven (CD), the inertia-driven but capillary-limited (IC) and the inertia-driven but viscous-limited (IV) regimes in more detail and present a prediction model for each regime. Note that the collision cases for a flat surface ($\Omega = 1/10$) are chosen first for demonstrating our results owing to its generality. Then we further extend our analysis considering the effect of the droplet-to-target size ratio (Ω).

We first examine the spreading time for the CD regime ($We \leq 10^1$). At this low We region the spreading dynamics is primarily governed by its wetting nature and the associated capillary effect where surface wettability plays a dominant role. Therefore, the capillary time scale, t_c^*, can be an appropriate time scale for analyzing physical characteristics of the spreading time in this regime [16,19].

Figure 7(a), (b), and (c) depict the effects of We, θ_{eqi} and Oh on the spreading profiles, respectively. As seen in Fig.7(a), the spreading time (τ_c) basically decreases as We increases whereas the maximum value of β^* (denoted as β^*_{max} hereafter) increases with We. This result is natural because higher spreading velocity can be attained at the high We cases [19], thus a shorter spreading time is needed. Note that this is also consistent with the experimental observation of Lin *et al*. [19]. For the cases shown in Fig.7(a), τ_c , where We = 10 ($\tau_c = 0.69$), is about 21 % shorter compared to that for the case where We = 2 ($\tau_c = 0.87$). In Fig.7(b), as expected, the dominant effect of the surface wettability is seen. The droplet can spread for a longer time over the surface as θ_{eqi} decreases (i.e., as the surface becomes hydrophilic) and can attain a larger spreading extent as well owing to the strongly wettable nature of the hydrophilic surface. This result is also consistent with the existing experimental data [19,43]. For the cases shown in Fig.7(b), τ_c, where $\theta_{eqi} = 20°$ ($\tau_c = 1.38$), is almost double the case where $\theta_{eqi} = 160°$ ($\tau_c = 0.70$).

It is interesting to observe the effect of Oh on τ_c. As depicted in Fig.7(c), for relatively

519 low Oh cases (Oh ≤ 0.0104, see 4 dashed lines), no meaningful effect of Oh is seen because
520 the spreading process is primarily driven by the capillary effect and is also terminated by the
521 capillary limit due to the negligible role of the viscous resistance at such low Oh numbers
522 [16,40]. Note also that this trend is consistent with the existing experimental observation of
523 Lee *et al*. [15] who showed that there was no notable difference of the spreading time
524 between a water droplet (Oh ~ 0.0026) and a glycerol mixture (Oh ~ 0.0263, about 10 times
525 the viscosity of a water droplet) under the given surface conditions (θ_{eqi} =52° – 61°) in the
526 low We region (We < 2.5). Conversely, the spreading profiles start to be affected by Oh as Oh
527 further increases above Oh ≥ 0.0262 [see solid lines in Fig.7(c)] and the recoiling stages
528 disappear for much higher Oh cases (Oh ≥ 0.1049) owing to the significant viscous damping.
529 The interesting point is that no notable difference of τ_c can be found even for higher Oh cases
530 (τ_c is almost constant for the entire range of Oh). We found that this is because Oh primarily
531 affects the spreading velocity, not the spreading time, for the higher Oh region. To check the
532 effect of Oh on the spreading velocity in more detail, in Fig.7(d) and (e), we plot the non-
533 dimensional spreading velocity V_s^* (defined as $V_s^* = \beta^*_{max} / \tau_c$) and the non-dimensional
534 maximum spreading extent β^*_{max} for the cases shown in Fig.7(c), respectively. As seen, V_s^* is
535 nearly constant for the low Oh region (roughly where Oh ≤ 0.01), whereas it significantly
536 decreases as Oh increases in the high Oh region (Oh ≥ 0.05). Since the effect of Oh on β^*_{max}
537 (this result in Fig.7(e) is also consistent with the existing experimental result [16]) evidently
538 shows exactly the same trend as the effect of Oh on V_s^*, τ_c can be considered almost
539 independent of Oh for the entire range of Oh.

540 It is also interesting to compare the spreading mechanism for this CD regime with the
541 retraction mechanism for high-speed impact cases. In fact, both processes (i.e., spreading of
542 low-speed impact and retraction of high-speed impact) are presumably based on the same
543 physical mechanism, i.e., capillary-driven motion under viscous resistance. In the high-speed

544 impact case, at the beginning of the retraction stage (i.e., right after the maximum spreading
545 state), the droplet shows a severely deformed interfacial shape and its motion is almost
546 stopped. Then we begin to see the capillary-driven recoiling motion under viscous resistance,
547 to reduce its increased surface energy caused by surface deformation during the former
548 spreading stage [62]. Since the spreading stage in the CD regime is also driven by the
549 capillary effect under viscous resistance, one can expect that there should essentially and
550 naturally be consistent physical characteristics between the spreading behavior of the low-
551 speed impact in the CD regime and the retraction behavior of the high-speed impact cases.
552 We found that the spreading velocity in the CD regime analyzed in Fig.7(d) demonstrates the
553 same trend as the retraction characteristics which were experimentally observed by Bartolo *et*
554 *al*. [62]. They showed that the retraction rate of a droplet is not affected by Oh where Oh <
555 0.05, whereas it is strongly reduced as Oh increases where Oh > 0.05. Their result shows an
556 excellent agreement with our findings described in Figs.7(c) and (d).
557 In Fig.7 above, we observed the obvious effects of We and θ_{eqi} on τ_c, whereas the effect
558 of Oh can be negligible. Therefore, τ_c in the CD regime can be properly represented by We
559 and θ_{eqi} and we propose a prediction model:
560
561 $$\tau_c = \left(1.66 - 0.31\theta_{eqi}\right) \mathrm{We}^{-0.24} \quad (6)$$
562
563 In figure 8, a total of 600 τ_c data are plotted with the prediction model in Eq.(6). As seen,
564 all τ_c data for a range of We ≤ 10 can nearly be collapsed on the single curve (see black solid
565 line), regardless of Oh. Above the threshold of We ~ 10 (i.e., beyond the CD regime) τ_c
566 cannot be properly represented by Eq.(6).
567 We now examine the spreading time for the IC regime [We ≥ O(10^1) and Oh ≤ O(10^{-2})].
568 At this high We but low Oh region, the spreading dynamics is primarily dominated by the

strong inertial effect but terminated by the capillary limit [16,40,62]. Therefore, the capillary time scale, t_c^*, can still be applicable for this regime [16,19].

Figure 9(a) depicts the effect of We on the spreading profiles. τ_c first decreases as We increases for the CD regime (see 5 dashed lines) as shown in Fig.7(a) above, but it increases again if We further increases (We $\geq$ 30) as the collision dynamics sufficiently enter the IC regime (see 6 solid lines). This somewhat interesting result can be attributed to the severe deformation of the leading edge of the lamella and its relaxation phenomena [40]. As the droplet spreads over the surface the leading edge of the lamella continues deforming. The tip of the lamella is detached from the surface, and it also continues growing as a rim by consuming the liquid mass from the central region of the droplet [27,70]. Note that such a deformed rim plays an important role in determining the maximum wetting area [70] since the volume of the rim is not small [27] and the maximum wetting area is attained during the relaxation period of the rim [40]. Therefore, a more deformed shape at higher We leads to the longer relaxation time of the rim and eventually the longer spreading time. Fan *et al*. [73] also experimentally showed that the spreading time of a water droplet on a spherical target first decreases as We increases, then it again increases with We if We $\geq$ 36.5, showing an agreement with our results in Fig.9(a). However, the authors think it would be ideal if our physical interpretation of the underlying mechanism shown in Fig.(b) could also be confirmed by additional experiments.

Fig.9(b) illustrates such a deformation and relaxation process of the rim in more detail. For the relatively low We case (We = 20), as depicted on the left side of Fig.9(b), the droplet continues its spreading process until it reaches the maximum spreading state and no significant deformation of the lamella edge is observed because the spreading dynamics does not fully enter the IC regime yet. Conversely, for the high We case where We = 110 [see the right side of Fig.9(b)], a severe deformation of the rim detached from the surface is clearly

captured at $t_c^* = 0.60\tau_c$ (see black line). Then the rim begins its relaxation to reduce the surface energy and eventually reaches the maximum spreading state (see pink line). Note that the relaxation period takes quite a long time (about 40 % of τ_c in this case) eventually leading to the delayed τ_c.

Fig.9(c) and (d) show the effects of θ_{eqi} and Oh on the spreading profiles, respectively. As seen, no meaningful effect of θ_{eqi} on τ_c is observed, because the effect of the surface wettability is overwhelmed by the strong inertial effect during most of the spreading stage [27,41]. Although the surface wettability plays a non-negligible role in the spreading profiles near the maximum spreading state and after τ_c (i.e., during the retraction stage) where the spreading velocity and the associated inertial effect are at a minimal level, the effect of θ_{eqi} on τ_c is almost negligible until the droplet reaches nearly the maximum spreading state. For this case τ_c can be considered to be a constant value regardless of the surface wettability. The effect of Oh on τ_c is also not meaningful if Oh is sufficiently small. As seen in Fig.9(d), τ_c is not affected by Oh if Oh < 10^{-2} (see 3 solid lines, i.e., at IC regime), whereas τ_c decreases as Oh increases if Oh > 10^{-2} (see 3 dashed lines, i.e., beyond the IC regime). This result is also consistent with the existing result of Zhu *et al*. [46] who demonstrated that the spreading dynamics is independent of Oh for low Oh, whereas it is strongly affected by Oh for high Oh under similar We conditions as the present study (We ≥ 25). Their proposed threshold (Oh ~ 0.008) is also consistent with the current observation (Oh ~ 0.01).

In Fig.9 above, we observed the obvious effect of We on τ_c, whereas the effects of θ_{eqi} and Oh can be negligible. Therefore, τ_c in the IC regime can be properly represented by We and we propose a prediction model:

$$\tau_c = 0.31\mathrm{We}^{0.18} \tag{7}$$

In figure 10, a total of 150 τ_c data are plotted with the prediction model in Eq.(7). As seen, all τ_c data for a range of We > 30 can nearly be collapsed on the single curve (see black solid line) regardless of θ_{eqi} and Oh.

We now examine the spreading time for the IV regime [We ≥ O(10^1) and Oh ≥ O(10^{-2})]. At this high We and Oh region the spreading dynamics is primarily dominated by the strong inertial effect but terminated by the viscous limit [16,40,62]. Therefore, the viscous time scale, t_v^*, would be the proper scale in this regime.

Figure 11(a), (b), and (c) depict the effects of We, θ_{eqi}, and Oh on the spreading profiles, respectively. As seen in Fig.11(a), the spreading time, τ_v, naturally decreases as We increases due to the higher spreading velocity [19]. The delayed spreading time shown in the IC regime (caused by the relaxation period of the deformed lamella rim) is not observed in this IV regime because the interfacial deformation is significantly restricted by the strong viscous damping. No meaningful effect of θ_{eqi} on τ_v is seen [see Fig.11(b)] due to its minor role compared to the strong inertial and viscous effects. Conversely, as expected, the dominant effect of Oh on τ_v is obviously detected in Fig.11(c). Since the spreading stage is terminated much earlier for higher Oh cases under the given We due to increased viscous resistance (i.e., the initial kinetic energy is more quickly dissipated [44]), τ_v is significantly reduced for higher Oh conditions. Note that the effect of Oh on τ_v observed in Fig.11(c) is also consistent with the existing experimental observation [19,44].

In Fig.11 above, we observed the obvious effects of We and Oh on τ_v, whereas the effect of θ_{eqi} can still be negligible. Therefore, τ_v in the IV regime can be properly represented by We and Oh, and we propose a prediction model:

$$\tau_v = 0.3\mathrm{Oh}^{-1.13}\mathrm{We}^{-0.22} \tag{8}$$

In figure 12, a total of 250 τ_v data are plotted with the prediction model in Eq.(8). As seen, all τ_v data for a range of We > 30 can nearly be collapsed on the single curve (see black solid line), regardless of θ_{eqi}.

D. Effect of target curvature and data-driven prediction model

In the above subsection, we addressed the effects of the three collision parameters (We, θ_{eqi}, and Oh) on the spreading time for the three different spreading regimes (CD, IC, and IV regimes) and a prediction model was presented for each regime for the cases where $\Omega = 1/10$ (for a flat surface). We now expand our analysis considering the surface curvature which has been relatively less explored. The effect of the target curvature characterized by the droplet-to-target size ratio (Ω) on the spreading time and a new prediction model for the spreading time which can be applied to the entire range of the 4 collision parameters will be presented in this subsection.

Figure 13(a), (b), and (c) depict the effects of Ω on the spreading profiles for the CD, the IC, and the IV regime, respectively. In the CD regime, as seen in Fig.13(a), τ_c increases with Ω (on the smaller target). This behavior is attributed to the reduced capillary force acting near the contact line for the smaller targets. As described above, at this low We level, the dominant force driving the spreading process is the capillary force F_c [which can be scaled as $F_c \sim \sigma R_w(\theta_{ap} - \theta_{eqi})$] formed at the initial stage of contact. At the instant that a droplet contacts a solid surface, its apparent contact angle (θ_{ap}) is almost close to 180° and the difference between the apparent contact angle and the equilibrium contact angle results in the capillary force F_c on the contact line. Since such an apparent contact angle at the initial contact stage is formed at a lower level on the smaller target [see θ_{ap2} and yellow dashed line in the zoom-in of the dashed black box, in Fig.13(d)] compared to the bigger target (see θ_{ap1}), $\theta_{ap} - \theta_{eqi}$ and F_c are reduced on the smaller targets eventually leading to lower spreading velocity and

669 longer spreading time. For the cases shown in Fig.13(a), τ_c where $\Omega = 1/2$ ($\tau_c = 0.99$) is about
670 21 % longer compared to that for the flat surface ($\Omega = 1/10$, $\tau_c = 0.82$).
671 As seen in Fig.13(b), the effect of Ω on τ_c is apparently observed also in the IC regime,
672 i.e., τ_c increases on the smaller targets. Note that the trend of the effect of Ω on τ_c in the IC
673 regime is also consistent with many existing studies [40,46,47] and this behavior is attributed
674 to the reduced lamella deformation on the smaller target [40]. As already shown in Fig.3(b)
675 above, a thin lamella sheet is ejected at the early stage of spreading. Although the motion of
676 bulk liquid is primarily dominated by inviscid inertial effects [16,40,62], the dynamics in the
677 vicinity of the lamella jet is locally but considerably affected by viscous effects [20,69]. Since
678 the smaller targets provide more space in the vertical direction as in an expanding channel
679 flow for the lamella sheet being ejected [i.e., higher ζ is provided on smaller targets as
680 illustrated in the zoom-in of the dashed red box in Fig.13(d)] the local velocity of the radially
681 expanding lamella jet is reduced on the smaller targets. Therefore, the lamella jet develops
682 less sharply, having a more rounded and bluff shape [40,69]. This allows the droplet to
683 expend its kinetic energy more efficiently for the spreading itself rather than the rim
684 deformation detached from the surface eventually leading to the longer spreading time as
685 well as the longer spreading extent compared to those on the larger targets (under the same
686 kinetic energy level). A more detailed physical mechanism for the reduced lamella
687 deformation on smaller targets can be found in the existing numerical study [40]. For the
688 cases shown in Fig.13(b), τ_c, where $\Omega = 1/2$ ($\tau_c = 0.80$) is about 45 % longer compared to that
689 for the flat surface ($\Omega = 1/10$, $\tau_c = 0.55$).
690 The effect of Ω on τ_v in the IV regime is depicted in Fig.13(c). As seen, no meaningful
691 effect of Ω on τ_v is observed for this highly viscous regime. Although the maximum
692 spreading extent is slightly increased on the smaller targets due to the reduced energy
693 dissipation [40], τ_v is almost constant in terms of its practical measurement.

In figure 14, we refine the regime map (shown in Fig.2 above) to summarize the major findings presented so far, including the details of the physical behaviors of the spreading time. The underlying physical mechanism governing the spreading process, the characteristic time scale, the effects of various collision parameters on the spreading time and the prediction model (for a flat surface) are also presented for each regime. Note that the effects of 4 collision parameters, i.e., We, θ_{eqi}, Oh, and Ω are indicated by 4 different markers, i.e., circles, squares, triangles and inverted triangles, respectively. If a certain parameter has a positive (or negative) effect on the spreading time, its effect is indicated by a red (or blue) marker, whereas an empty marker is used if its effect is negligible. For example, if the spreading time increases with We, the effect of We is marked by a filled red circle. Conversely, the effect of We is marked by a filled blue circle if the spreading time decreases as We increases.

Fig.14 highlights the complex nature of the spreading time owing to the different physical mechanism for each regime. The effects of the impact parameters (We, θ_{eqi}, Oh and Ω) also play different roles. For instance, the effect of We is positively related to the spreading time for the CD and the IV regime, whereas it is negatively related to the spreading time for the IC regime. In particular, none of the 4 impact parameters shows a consistent effect across the three spreading regimes, which highlights the significant nonlinearity and complexity of the spreading time. The characteristic time scales are also different.

Therefore, formulating a single correlation for the spreading time as a broad cross-over across the three different spreading regimes is quite difficult since it should cover all the different physical mechanisms, different characteristic time scales, and different effects of the collision parameters. In addition, if the effect of the target curvature (i.e., the effect of Ω) on the spreading time were to be considered together, the problem would be much more complicated. Rather than formulating a single correlation, therefore, we consider here a data-

719 driven approach to model such complex and non-linear behavior of the spreading time across
720 all the spreading regimes.
721 Recently, data-driven approaches have been broadly applied to model complicated fluid
722 phenomena such as turbulent flows [74] or multiphase flow systems [75]. For droplet impact
723 problems as well, the maximum spreading extent [41], the splashing threshold [76], and the
724 lamella area [77] have successfully been modeled using data-driven techniques, based on
725 their powerful ability to correlate non-linear relations among large datasets and reduce the
726 level of complexity.
727 The spreading time can basically be modeled as a function of 4 impact parameters as
728 follows:
729
730 $$\tau_a = f(\mathrm{We}, \mathrm{Oh}, \theta_{eqi}, \Omega) \quad (9)$$
731
732 Here, the advective time scale is applied for our data-driven prediction model, in order to
733 treat our dataset in a consistent manner. f is the non-linear and complicated (unknown)
734 function between inputs (4 impact parameters) and output (τ_a) data which is now modeled by
735 using an artificial intelligence technique. The multilayer neural network, also called the
736 multilayer perceptron (MLP) [78], is utilized as a nonlinear regressor to model the function f.
737 Figure 15 illustrates the schematic diagram of the typical MLP structure. The MLP consists of
738 the input layer (marked by red nodes), the multiple hidden layers (marked by green nodes)
739 and the output layer (marked by blue nodes). Each layer usually consists of a number of
740 nodes (also called neurons), whereas the last output layer has only one output node. The 4
741 input features (We, Oh, θ_{eqi} and Ω) are provided from the input layer to the first hidden layer
742 and then linear combinations of the input features are calculated on each node. Such linear
743 combinations are nonlinearized by using an activation function and then are delivered to the

744 next hidden layer. Such an operation is called a feedforward procedure and is applied to all
745 the subsequent layers. The last output layer has no nonlinearization operation and provides
746 the final output value.

747 A total of 2400 impact cases (12 Weber numbers, 10 Ohnesorge numbers, 5 surface
748 wettabilities, and 4 droplet-to-target size ratios) are utilized to set the dataset. The dataset is
749 randomly split into 3 parts: the training dataset (70 %, 1680 data points), the validation
750 dataset (15 %, 360 data points) and the test dataset (15 %, 360 data points). The training
751 dataset and the test dataset are used to train our MLP model and finally test the accuracy of
752 the trained model, respectively, whereas the validation dataset is utilized to check if
753 overfitting occurs during the training process. More detailed information on our MLP
754 modeling and its training procedure can be found in the Appendix C.

755 Figure 16 compares the spreading time predicted by our data-driven model with the true
756 values (measured values from our numerical simulations). 360 data points from the test
757 dataset are plotted for comparison (see black circles). As can be seen, τ_a predicted by our
758 MLP model demonstrates a good agreement with the true dataset, showing that the mean
759 square error (MSE) is on the order of $O(10^{-4})$ ($MSE = 5.23 \times 10^{-4}$). Note that, except for only
760 a few cases, all the tested cases fall inside a deviation range of ± 15%. Note that all the test
761 data samples shown in Fig.16 have not been used for the training process of our MLP model.
762 To the best of our knowledge, our prediction model is the first data-driven model for the
763 spreading time of the droplet collision system which can be applied for a curved spherical
764 target. As one of the most universal models, the current model can cover a very broad range
765 of impact parameters across not only the three spreading regimes (i.e., CD, IC, IV regimes
766 and the transition area among them as well), but also a wide range of droplet-to-target size
767 ratio (from a flat substrate to a small spherical target).

768 Last but not least, the authors would like to clarify that there is no physics in the current

data-driven prediction model, which can indeed be understood as providing both pros and cons [75]. The fact that such a data-driven approach is not fully based on a physical background might be a reason for which it has been less attractive to some scientific communities compared to conventional approaches supported by strong physical principles [79,80]. However, both approaches share identical goals, i.e., modeling complicated phenomena which usually need to consider many multi-dimensional variables [80,81]. The advantages of data-driven approaches can also be that users would not need to consider physics models alone for those complex system because data-driven models basically don't rely on constraints attributed to physics [75]. This characteristic allows them to work as a useful non-linear regressor. For example, the current data-driven prediction model can predict the spreading time even for transition regimes marked in the gray zones in Fig.14, which is apparently very difficult to predict using Eqs. 6 – 8 above due to their non-linear nature. This clearly shows the advantage of data-driven approaches at least in the context of engineering applications and practical usefulness.

IV. CONCLUSION

In this study we quantitatively and systematically investigate the spreading time of droplet impact onto a spherical target for a wide range of impact parameters ($0 \leq We \leq 110$, $20° \leq \theta_{eqi} \leq 160°$, $0.0013 \leq Oh \leq 0.7869$ and $1/10 \leq \Omega \leq 1/2$). A total of 2400 collision cases are simulated and are used to better understand the physical behavior of the spreading time. This large simulation dataset is also used for training a data-driven prediction model as well as for the derivation of prediction models.

For the three different spreading regimes, i.e., the capillary-driven (CD), the inertia-

793 driven but capillary-limited (IC) and the inertia-driven but viscous-limited (IV) regimes, the
794 effects of the impact parameters on the spreading time are analyzed in detail. Not only the
795 spreading time, but also proper time scales, dominant impact parameters and associated
796 physical behaviors all significantly and non-linearly change across the three spreading
797 regimes. The spreading time is primarily dominated by the We and θ_{eqi} in the CD regime
798 whereas only the Weber number plays a meaningful role in the IC regime. In the IV regime it
799 is mainly affected by We and Oh. An improved prediction model is also presented for each
800 regime. To the best of our knowledge, these proposed prediction models (Eqs. 6-8) are the
801 first models for the spreading time using only the controllable independent variables (e.g.,
802 We, Oh and θ_{eqi}) in explicit form which can provide more straightforward solutions compared
803 to the existing models [18-21,44,45].
804 The effect of target curvature on the spreading time is also analyzed in detail for the
805 three different spreading regimes, showing complicated trends due to its non-linear nature.
806 Finally, a data-driven prediction model is proposed to predict the spreading time broadly
807 across the three different spreading regimes. Our proposed data-driven model shows good
808 prediction capability for the full ranges of impact parameters considered in the present study
809 and also shows a good agreement with our simulation dataset.
810 The limitation of the current study is as follows: (i) As in the existing models, prediction
811 models (Eqs. 6-8) are still not derived from physical background. Further efforts are needed
812 to combine "physics-based models" which could be helpful in understanding such
813 complicated behavior within the existing empirical results. (ii) Users need to be careful in
814 using the proposed data-driven model. Although our numerical methods have thoroughly
815 been validated, the number of current data samples (2400 cases) is still insufficient to model
816 the spreading time for the entire spreading regime compared to other common data-driven
817 models trained using "big-data". Our numerical data used for the training are also confined to

the current impact conditions ($0 \le We \le 110$, $20° \le \theta_{eqi} \le 160°$, $0.0013 \le Oh \le 0.7869$ and $1/10 \le \Omega \le 1/2$). Broader ranges of impact parameters, and more precise and abundant data samples can improve the applicability and accuracy of the current model. (iii) While the current axi-symmetric simulation code is sufficiently validated, full three-dimensional simulations are still essential to better understand those complicated physical phenomena. In particular, impact dynamics at high We and low Oh where the liquid sheets and rim can be highly deformed still need to be captured more precisely. We are currently working on these issues.

APPENDIX A: Details of the dynamic contact angle modeling

The dynamic contact angle θ_{dyn} is basically modeled as a function of the equilibrium contact angle and the velocity of the contact line, as in well-known previous numerical studies on drop impact problems [82,83]. In the present study, we use the model of Yokoi *et al*. [83]:

$$\theta_{\mathrm{dyn}}\left(U_{CL}\right)=\begin{cases}\min\left[\theta_{\mathrm{eqi}}+\left(\dfrac{\mathrm{Ca}}{q_1}\right)^{1/3},\ \theta_{\mathrm{mda}}\right], & \text{if } U_{\mathrm{CL}}\ge 0 \ \text{(for spreading)}\\ \max\left[\theta_{\mathrm{eqi}}+\left(\dfrac{\mathrm{Ca}}{q_2}\right)^{1/3},\ \theta_{\mathrm{mdr}}\right], & \text{if } U_{\mathrm{CL}}\le 0 \ \text{(for receding).}\end{cases} \tag{A1}$$

Ca is the capillary number ($\mathrm{Ca} = \mu U_{\mathrm{CL}}/\sigma$), where U_{CL} is the velocity of the contact line. Contact angle hysteresis is represented by the difference between the allowable minimum

(θ_{mdr}) and maximum (θ_{mda}) contact angles, and the dynamic contact angle (θ_{dyn}) can always be maintained between θ_{mdr} and θ_{mda}. q_1 and q_2 are experimentally measured constants, and the same values as in Yokoi *et al.* [83] ($q_1 = 9.0 \times 10^{-9}$ and $q_2 = 9.0 \times 10^{-8}$) are applied to the current study.

APPENDIX B: Validation tests in our previous studies

We here introduce our validation test results presented in our previous studies. Figure 17(a) compares the maximum spreading extent β^*_{max} computed by our simulation with Mao *et al.* [25]'s semi-empirical model which is well-known as one of the most accurate models that can be applied for a wide range of drop viscosity [84]. β^*_{max} shows generally good agreement with the existing model of Mao *et al*. [25] for a wide range of We number ($30 \leq We \leq 90$) and Oh number ($0.0013 \leq Oh \leq 0.7869$). Note that a discrepancy shown at the very low Oh region ($Oh \leq 0.0026$) is attributed to the limitation of shape approximation in Mao *et al*.'s model [25], which overestimates β^*_{max} if the viscosity is very low and the surface tension force plays an important role [25,84]. Therefore, in figure 17(b), we compare our simulated β^*_{max} again with the well-known viscous-free scaling law proposed by Clanet *et al*. [16]. As can be seen, for cases with very low Oh number ($Oh = 0.0026$), our simulation result shows an excellent agreement with the existing scaling law [16].

In figure 17(c), we further compare our simulated time-dependent non-dimensional spreading diameter β^* with three existing experimental results to see if our numerical framework can simulate the impact phenomena well on spherical targets. The solid lines in Fig. 17(c) depict the simulation results, whereas the red squares, blue circles, and black crosses show the experimental results from Mitra *et al*. [2], Liu *et al*. [38], and Khurana *et al*. [39], respectively. Our simulation results also show good agreement with the existing

experimental observations in the literature, in the context of dynamic spreading characteristics. Overall, we concluded that our simulation framework can simulate the drop impact phenomena on both flat and spherical targets well for a wide range of collision parameters. Note again that these validation tests shown in figure 17 are not new tests, but were already presented in our previous study [40].

APPENDIX C: Details of MLP training

The output value on the n^{th} node in the m^{th} layer is:

$$a_n^m = g\left(\sum_{k=1}^{N^{m-1}} w_{nl}^m a_l^{m-1} + b_n^m\right) \tag{C1}$$

Here, N stands for the number of nodes of each layer. The function g denotes the nonlinear activation function. w_{nl} is the weight between the l^{th} node of the previous layer and the n^{th} node of the current layer whereas b is the bias.

The weights (w) and biases (b) are adjustable coefficients and are first initialized as random variables and zero, respectively. w and b are continuously updated during the training process, minimizing the loss function based on the back-propagation algorithm [85]. In the current study, the mean square error (MSE) is used as a loss function:

$$\mathrm{MSE} = \frac{1}{M}\sum_{k=1}^{M}\left(\tau_a - \tau_{a(\mathrm{p})}\right)^2 \tag{C2}$$

where M is the number of data points considered and $\tau_{a(\mathrm{p})}$ is the predicted value of the

spreading time using the trained MLP model.

Three hyperparameters (i.e., the activation function, the number of nodes at each hidden layer and the number of hidden layers) can usually be selected by the user. We chose the common rectified linear unit function (generally called ReLU) as our activation function owing to its well-known capability for deep neural networks [86]. The ReLU can be written as:

$$g(x) = \mathrm{ReLU}(x) = \max(x, 0) \tag{C3}$$

Two other hyperparameters are set by manual search because the current dataset is relatively very simple. Finally, a 4 × 30 (4 hidden layers and 30 neurons in each hidden layer) architecture is chosen as the MLP network. The ADAM optimization procedure [87,88] is used for the MLP training and the computational implementation for the MLP training is performed using the open-source libraries Keras [89] and TensorFlow [90]. For more details on the deep learning architecture and its training techniques readers can refer to Nielsen [91].

The training of our MLP model is carried out until the validation MSE (measured from the validation dataset) reaches a steady state. After 3300 training epochs the validation MSE converges to a steady state of about 4.62×10^{-4} (see Fig.18).

DECLARATIONS

Ethical Approval

Not applicable.

Conflict of interest

The authors declare that they have no conflict of interest.

Authors' contributions

Ikroh Yoon led conceptualization, data curation, formal analysis, investigation, validation, visualization, and writing (draft). Seungwon Shin led funding acquisition, methodology, resources, and software, and supported conceptualization, data curation, formal analysis, investigation, validation, visualization, and writing (draft). Damir Juric and Jalel Chergui supported conceptualization, data curation, formal analysis, funding acquisition, investigation, methodology, resources, software, validation, visualization, and writing (draft). All authors equally contributed to reviewing/editing the manuscript.

Funding

This work was supported by the National Research Foundation of Korea (NRF) grant funded by the Korea government (MSIT) (RS-2023-00244322) and support through computing time at the Institut du Developpement et des Ressources en Informatique Scientifique (IDRIS) of the Centre National de la Recherche Scientifique (CNRS), coordinated by GENCI (Grand Equipement National de Calcul Intensif) Grant 2023 A0142B06721.

Data availability

The data that support the findings of this study are available from the corresponding author, I. Yoon, upon reasonable request.

References

1. D. Khojasteh, N. M. Kazerooni, and M. Marengo, “A review of liquid droplet impacting onto solid spherical particles: A physical pathway to encapsulation mechanisms,” J. Ind. Eng. Chem. **71**, 50–64 (2019).

2. S. Mitra, G. M. Evans, E. Doroodchi, V. Pareek, and J. B. Joshi, “Interactions in droplet and particle system of near unity size ratio,” Chem. Eng. Sci. **170**, 154–175 (2017).

3. J. D. Oxley, "5 - Spray cooling and spray chilling for food ingredient and nutraceutical encapsulation," Encapsulation Technologies and Delivery Systems for Food Ingredients and Nutraceuticals, Woodhead Publishing, 110-130 (2012).

4. V. Nedovic, A. Kalusevic, V. Manojlovic, S. Levic and B. Bugarski, "An overview of encapsulation technologies for food applications," Procedia Food Sci. **1**, 1806-1815 (2011).

5. T. Chien and H. Chu, "Removal of SO2 and NO from flue gas by wet scrubbing using an aqueous NaClO2 solution," J. Hazard. Mater. **80** (1–3), 43-57 (2000).

6. E. Teunou, and D. Poncelet, "Batch and continuous fluid bed coating – review and state of the art," Journal of Food Engineering, **53** (4), 325-340 (2002).

7. A. Kundu, K. D. P. Nigam and R. P. Verma, "Catalyst wetting characteristics in trickle-bed reactors," AIChE J. **49** (9), 2253-2263 (2003).

8. B. Moon, N. Abbasi, S. G. Jones, D. K. Hwang and S. S. H. Tsai, "Water-in-Water Droplets by Passive Microfluidic Flow Focusing," Anal. Chem. **88** (7), 3982-3989 (2016).

9. D. A. Bolleddula, A. Berchielli and A. Aliseda, "Impact of a heterogeneous liquid droplet on a dry surface: Application to the pharmaceutical industry," Advances in Colloid and Interface Science, **159** (2) 144-159 (2010).

10. G. Charalampous and Y. Hardalupas, "Collisions of droplets on spherical particles," Phys. Fluids **29**, 103305 (2017).

11. S. Sohrabi, N. kassir, and M. K. Moraveji, "Retracted Article: Droplet microfluidics: fundamentals and its advanced applications," RSC Adv. **10** (46) 27560-27574 (2020).

12. C. Josserand and S. T. Thoroddsen, "Drop impact on a solid surface," Annu. Rev. Fluid Mech. **48**, 365–391 (2016).

13. A. L. Yarin, "Drop Impact Dynamics: Splashing, Spreading, Receding, Bouncing, ...," Annu. Rev. Fluid Mech. **38**, 159 (2006).

14. C. Antonini, A. Amirfazli, and M. Marengo, “Drop impact and wettability: From hydrophilic to superhydrophobic surfaces,” Phys. Fluids **24**, 102104 (2012).

15. J. B. Lee, N. Laan, K. G. De Bruin, G. Skantzaris, N. Shahidzadeh, D. Derome, J. Carmeliet, and C. Bonn, “Universal rescaling of drop impact on smooth and rough surfaces,” J. Fluid Mech. **786**, R4 (2016).

16. C. Clanet, C. Béguin, D. Richard, and D. Quéré, “Maximal deformation of an impacting drop,” J. Fluid Mech. **517**, 199–208 (2004).

17. S. Wildeman, C. Visser, C. Sun, and D. Lohse, “On the spreading of impacting drops,” J. Fluid Mech. **805**, 636–655 (2016).

18. H. Huang and X. Chen, "Energetic analysis of drop’s maximum spreading on solid surface with low impact speed", Phys. Fluids **30**, 022106 (2018).

19. S. Lin, B. Zhao, S. Zou, J. Guo, Z. Wei, and L. Chen, "Impact of viscous droplets on different wettable surfaces: Impact phenomena, the maximum spreading factor, spreading time and post-impact oscillation," Journal of Colloid and Interface Science, **516**, 86-97 (2018).

20. Y. T. Aksoy, P. Eneren, E. Koos, and M. R. Vetrano, "Spreading of a droplet impacting on a smooth flat surface: How liquid viscosity influences the maximum spreading time and spreading ratio," Phys. Fluids. **34**, 042106 (2022).

21. Du, X. Wang, Y. Li, Q. Min, and X. Wu, "Analytical Consideration for the Maximum Spreading Factor of Liquid Droplet Impact on a Smooth Solid Surface," Langmuir 37, 7582-7590 (2021).

22. J. Ancheyta, “Modeling and Simulation of Catalytic Reactors for Petroleum Refining,” Wiley, (2011).

23. S. Chandra and C. T. Avedisian, “On the collision of a droplet with a solid surface,” Proc. R. Soc. London A **432**, 13 (1991).

24. M. Pasandideh-Fard, Y. Qiao, S. Chandra, and J. Mostaghimi, “Capillary effects during droplet impact on a solid surface,” Phys. Fluids **8**, 650 (1996).

25. T. Mao, D. Kuhn, and H. Tran, “Spread and rebound of liquid droplets upon impact on flat surfaces,” AIChE J. **43**, 2169–2179 (1997).

26. C. Ukiwe and D. Y. Kwok, “On the maximum spreading diameter of impacting droplets on well-prepared solid surfaces,” Langmuir **21**, 2, 666–673 (2005).

27. I. V. Roisman, “Inertia dominated drop collisions. II. An analytical solution of the Navier–Stokes’s equations for a spreading viscous film,” Phys. Fluids **21**, 052104 (2009).

28. N. Laan, K. G. de Bruin, D. Bartolo, C. Josserand, and D. Bonn, "Maximum Diameter of Impacting Liquid Droplets,", Phys. Rev. Applied **2**, 044018 (2014).

29. J. Eggers, M. A. Fontelos, C. Josserand, and S. Zaleski, “Drop dynamics after impact on a solid wall: Theory and simulations,” Phys. Fluids **22**, 062101 (2010).

30. I. V. Roisman, R. Rioboo, and C. Tropea, “Normal impact of a liquid drop on a dry surface: Model for spreading and receding,” Proc. R. Soc. Lond. A. **458**, 1411–1430 (2002).

31. S. Bakshi, I. V. Roisman, and C. Tropea, “Investigations on the impact of a drop onto a small spherical target,” Phys. Fluids **19**, 032102 (2007).

32. I. Malgarinos, N. Nikolopoulos, and M. Gavaises, “A numerical study on droplet-particle collision dynamics,” Int. J. Heat Fluid Flow **61**, 499–509 (2016).

33. I. Malgarinos, N. Nikolopoulos, and M. Gavaises, "Numerical investigation of heavy fuel droplet-particle collisions in the injection zone of a Fluid Catalytic Cracking reactor, part II: 3D simulations,", Fuel Processing Technology 156, 43-53 (2017).

34. D. Zhang, K. Papadikis, and S. Gu, “Investigations on the Droplet Impact onto a Spherical Surface with a High Density Ratio Multi-Relaxation Time Lattice-Boltzmann Model,” Communications in Computational Physics **16** (4), 892-912 (2014).

35. D. Zhang, K. Papadikis, and S. Gu, “Application of a high density ratio lattice-Boltzmann model for the droplet impingement on flat and spherical surfaces,” Int. J. Therm. Sci. **84**, 75–85 (2014).

36. G. Liang, Y. Guo, X. Mu, S. Shen, "Experimental investigation of a drop impacting on wetted spheres," Experimental Thermal and Fluid Science 55, 150-157 (2014).

37. S. Mitra, T. B. T. Nguyen, E. Doroodchi, V. Pareek, J. B. Joshi, and G. M. Evans, “On wetting characteristics of droplet on a spherical particle in film boiling regime,” Chem. Eng. Sci. **149**, 181–203 (2016).

38. X. Liu, X. Zhang, and J. Min, “Maximum spreading of droplets impacting spherical surfaces,” Phys. Fluids. **31**, 092102 (2019).

39. G. Khurana, N. Sahoo, and P. Dhar, “Phenomenology of droplet collision hydrodynamics on wetting and non-wetting spheres,” Phys. Fluids **31**, 072003 (2019).

40. I. Yoon and S. Shin, “Maximal spreading of droplet during collision on particle: effects of liquid viscosity and surface curvature,” Phys. Fluids **33**, 083310 (2021).

41. I. Yoon, J. Chergui, D. Juric, and S. Shin, “Maximum spreading of droplet-particle collision covering a low Weber number regime and data-driven prediction model,” Phys. Fluids **34**, 102109 (2022).

42. D. Richard, C. Clanet, and D. Quéré, “Contact time of a bouncing drop,” Nature **417**, 811 (2002).

43. D. C. Vadillo, A. Soucemarianadin, C. Delattre, and D. C. D. Roux, "Dynamic contact angle effects onto the maximum drop impact spreading on solid surfaces,” Phys. Fluids **21**, 122002 (2009).

44. J. B. Lee, D. Derome, R. Guyer, and J. Carmeliet, "Modeling the Maximum Spreading of Liquid Droplets Impacting Wetting and Nonwetting Surfaces," Langmuir **32**, 1299-1308 (2016).

45. F. Wang, L. Yang, L. Wang, Y. Zhu, and T. Fang, "Maximum Spread of Droplet Impacting onto Solid Surfaces with Different Wettabilities: Adopting a Rim–Lamella Shape," Langmuir **35**, 3204-3214 (2019).

46. Y. Zhu, H. Liu, K. Mu, P. Gao, H. Ding, and X. Lu, “Dynamics of drop impact onto a solid sphere: Spreading and retraction.” J. Fluid Mech. **824**, R3 (2017).

47. X. Liu, J. Min, X. Zhang, Z. Hu, and X. Wu, "Supercooled water droplet impacting-freezing behaviors on cold superhydrophobic spheres," Int. J. Multiph. Flow **141**, 103675 (2021).

48. I. Yoon and S. Shin, “Direct numerical simulation of droplet collision with stationary spherical particle: A comprehensive map of outcomes,” Int. J. Multiph. Flow **135**, 103503 (2021).

49. I. Yoon, C. Ha, C. Lee, and S. Shin, "Promoting rebound from droplet impact on a spherical particle: Experimental and numerical study," Phys. Fluids **34**, 103302 (2022).

50. J. Han, W. Kim, C. Bae, D. Lee, S. Shin, Y. Nam, and C. Lee, “Contact time on curved superhydrophobic surfaces,” Phys. Rev. E **101**, 043108 (2020)**.**

51. I. Yoon, J. Chergui, D. Juric, and S. Shin, “Adaptive mesh axi-symmetric simulation of droplet impact with a spherical particle in mid-air,” Int. J. Multiph. Flow **155**, 104193 (2022).

52. S. Shin, J. Chergui, and D. Juric, “A solver for massively parallel direct numerical simulation of three-dimensional multiphase flows,” J. Mech. Sci. Technol. **31**, 1739–1751 (2017).

53. J.U. Brackbill, D.B Kothe and C. Zemach, "A continuum method for modeling surface tension," J. Comput. Phys. **100** (2), 335-354 (1992).

54. S. Unverdi, and G. Tryggvason, “A front-tracking method for viscous, incompressible, multi-fluid flows,” J. Comput. Phys. **100**, 25–37 (1992).

55. S. Shin, and D. Juric, “Modeling three-dimensional multiphase flow using a level contour reconstruction method for front tracking without connectivity,” J. Comput. Phys. **180**, 427–470 (2002).

56. S. Shin and D. Juric, “A hybrid interface method for three-dimensional multiphase flows based on front tracking and level set techniques,” Int. J. Numer. Meth. Fluids **60,** 753–778 (2009).

57. S. Shin, J. Chergui, and D. Juric, “Direct simulation of multiphase flows with modeling of dynamic interface contact,” Theor. Comput. Fluid Dyn. **32**, 655–687 (2018).

58. S. Osher and J. Sethian, “Fronts propagating with curvature-dependent speed: Algorithms based on Hamilton-Jacobi formulations,” J. Comput. Phys. **79**, 12–49 (1988).

59. C. Mundo, M. Sommerfield, and C. Tropea, “Droplet-wall collisions: experimental studies of the deformation and breakup process,” Int. J. Multiph. Flow **21**(2), 151–173 (1995).

60. L. Xu, W. W. Zhang, and S. R. Nagel, "Drop Splashing on a Dry Smooth Surface," Phys. Rev. Lett. **94** (18), 184505 (2005).

61. I. V. Roisman, E. Berberović, and C. Tropea, "Inertia dominated drop collisions. I. On the universal flow in the lamella,” Phys. Fluids **21**, 052103 (2009).

62. D. Bartolo, C. Josserand, and D. Bonn, “Retraction dynamics of aqueous drops upon impact on non-wetting surfaces”, J. Fluid Mech. **545**, 329–338 (2005).

63. Y. Hardalupas, A. M. K. P. Taylor and J. H. Wilkins, “Experimental investigation of sub-millimetre droplet impingement on to spherical surfaces,” Int. J. Heat Fluid Flow **20** (5), 477–485 (1999).

64. G. H. McKinley and M. Renardy, “Wolfgang von Ohnesorge,” Phys. Fluids. **23**, 127101 (2011).

65. B. R. Munson, D. F. Young, and T. H. Okiishi, *Fundamentals of Fluid Mechanics*, 5th ed. (John Wiley and Sons, New York, 2006)

66. A. Biance, F. Chevy, C. Clanet, G. Lagubeau, and D. Quéré, “On the elasticity of an inertial liquid shock,” J. Fluid Mech. **554** (1), 47–66 (2006).

67. J. Du, N. T. Chamakos, A. G. Papathanasiou, and Q. Min, "Initial spreading dynamics of a liquid droplet: The effects of wettability, liquid properties, and substrate topography,” Phys. Fluids. **33**, 042118 (2021).

68. Y. Renardy, S. Popinet, L. Duchemin, M. Renardy, S. Zaleski, C. Josserand, … and D. Quéré, “Pyramidal and toroidal water drops after impact on a solid surface,” J. Fluid Mech. **484**, 69-83 (2003).

69. A. Mongruel, V. Daru, F. Feuillebois, and S. Tabakova , "Early post-impact time dynamics of viscous drops onto a solid dry surface", Phys. Fluids **21**, 032101 (2009).

70. A. I. Fedorchenko, and A. B. Wang, “The formation and dynamics of a blob on free and wall sheets induced by a drop impact on surfaces,” Phys. Fluids **16**, 3911–3920 (2004).

71. S. A. Banitabaei and A. Amirfazli, “Droplet impact onto a solid sphere: Effect of wettability and impact velocity,” Phys. Fluids **29**, 062111 (2017).

72. Z. Jian, C. Josserand, S. Popinet, P. Ray and S. Zaleski, “Two mechanisms of droplet splashing on a solid substrate,” J. Fluid Mech. **835**, 1065-1086 (2018).

73. Z. Fan, D. Liu, S. Pan, J. Ma, and X. Chen, “Spreading dynamics of the viscous droplet impacting on a spherical particle,” Phys. Fluids **35**, 023311 (2023).

74. K. Duraisamy, G. Iaccarino, and H. Xiao, "Turbulence Modeling in the Age of Data," Annu. Rev. Fluid Mech. **51**, 357-377 (2019).

75. M. Ma, J. Lu, and G. Tryggvason, "Using statistical learning to close two-fluid multiphase flow equations for a simple bubbly system," Phys. Fluids. **27**, 092101 (2015).

76. M. Pierzyna, D. A. Burzynski, S. E. Bansmer, and R. Semaan, "Data-driven splashing threshold model for drop impact on dry smooth surfaces,” Phys. Fluids. **33**, 123317 (2021).

77. V. Vilela, F. J. de Souza, "A Numerical Study on Droplet-Particle Collision," Flow Turbulence Combust **105**, 965–987 (2020).

78. F. Rosenblatt, “The Perceptron, a perceiving and recognizing automaton project para,” Report Vol. **85**, Nos. 460–461, Cornell Aeronautical Laboratory (1957).

79. Y. He, D. Xiu, “Numerical strategy for model correction using physical constraints,” J. Comput. Phys. **313**, 617–634 (2016).

80. P. S. Koutsourelakis, N. Zabaras, and M. Girolami, "Special Issue: Big data and predictive computational modeling," J. Comput. Phys. **321**, 1252-1254 (2016).

81. P. Gelss, S. Matera, and C. Schuette, "Solving the master equation without kinetic Monte Carlo: tensor train approximations for a CO oxidation model," J. Comput. Phys. **314**, 489–502 (2016).

82. Š. Šikalo, H.-D. Wilhelm, I. V. Roisman, S. Jakirlić, and C. Tropea, "Dynamic contact angle of spreading droplets: Experiments and simulations," Phys. Fluids **17**, 062103 (2005).

83. K. Yokoi, D. Vadillo, J. Hinch, and I. Hutchings, "Numerical studies of the influence of the dynamic contact angle on a droplet impacting on a dry surface," Phys. Fluids **21**, 072102 (2009).

84. P. Attané, F. Girard, v. Morin, "An energy balance approach of the dynamics of drop impact on a solid surface," Phys. Fluids **19**, 012101 (2007).

85. D. E. Rumelhart, G. E. Hinton, and R. J. Williams, "Neurocomputing: Foundations of Research, Learning Representations by Back-propagating Errors" MIT Press (Cambridge, MA, USA, 1988), 696–699.

86. V. Nair, and G. E. Hinton, "Rectified linear units improve restricted Boltzmann machines," In: Proceedings of 27th International Conference on Machine Learning (2010).

87. D. P. Kingma and J. Ba, "Adam: A method for stochastic optimization," presented at the Third International Conference on Learning Representations, San Diego, CA, USA, 2015; e-print arXiv:1412.6980.

88. S. Ruder, “An overview of gradient descent optimization algorithms,” [cs.LG], 2017.

89. F. Chollet, “Keras,” (2015). https://keras.io.

90. Abadi, M. *et al*., “TensorFlow: Large-scale machine learning on heterogeneous systems,” (2015). Software available from https://www.tensorflow.org/

91. M. A. Nielsen, “Neural Network and Deep Learning,” Determination Press (2015).

FIGURES

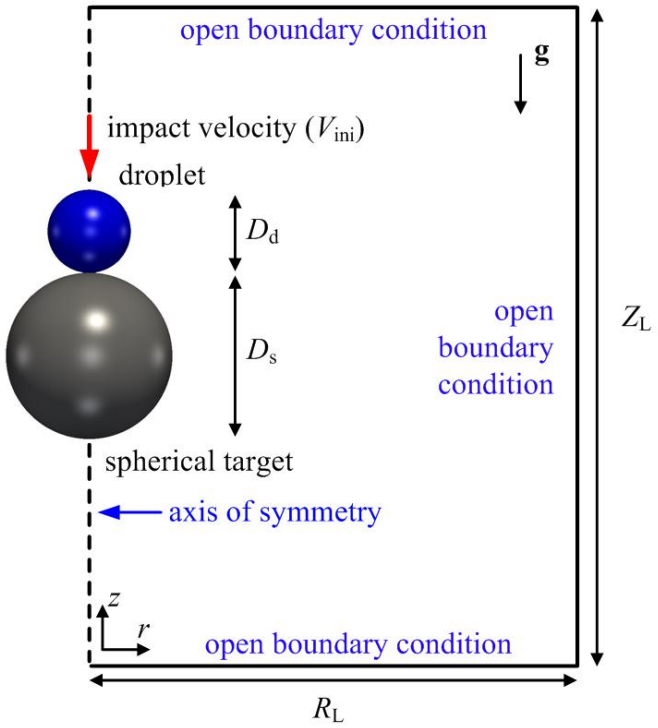

Fig. 1. Simulation geometry and boundary conditions for the droplet impact system.

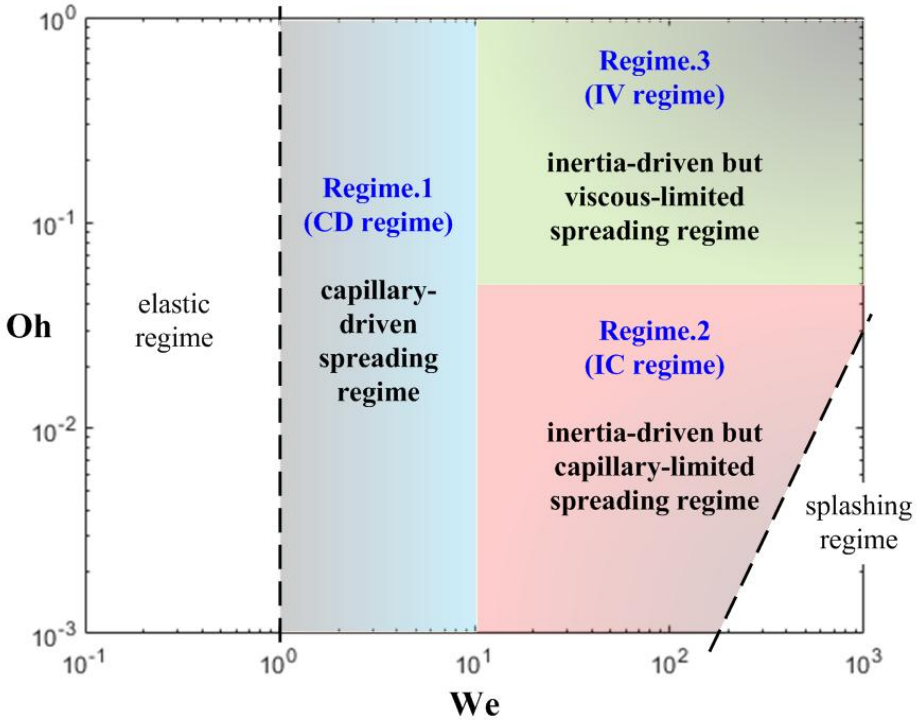

Fig. 2. Schematic regime-map for droplet spreading dynamics. Three different spreading regimes, i.e., the capillary-driven (CD), the inertia-driven but capillary-limited (IC), and the inertia-driven but viscous-limited (IV) regimes are marked by the blue, red and green areas, respectively.

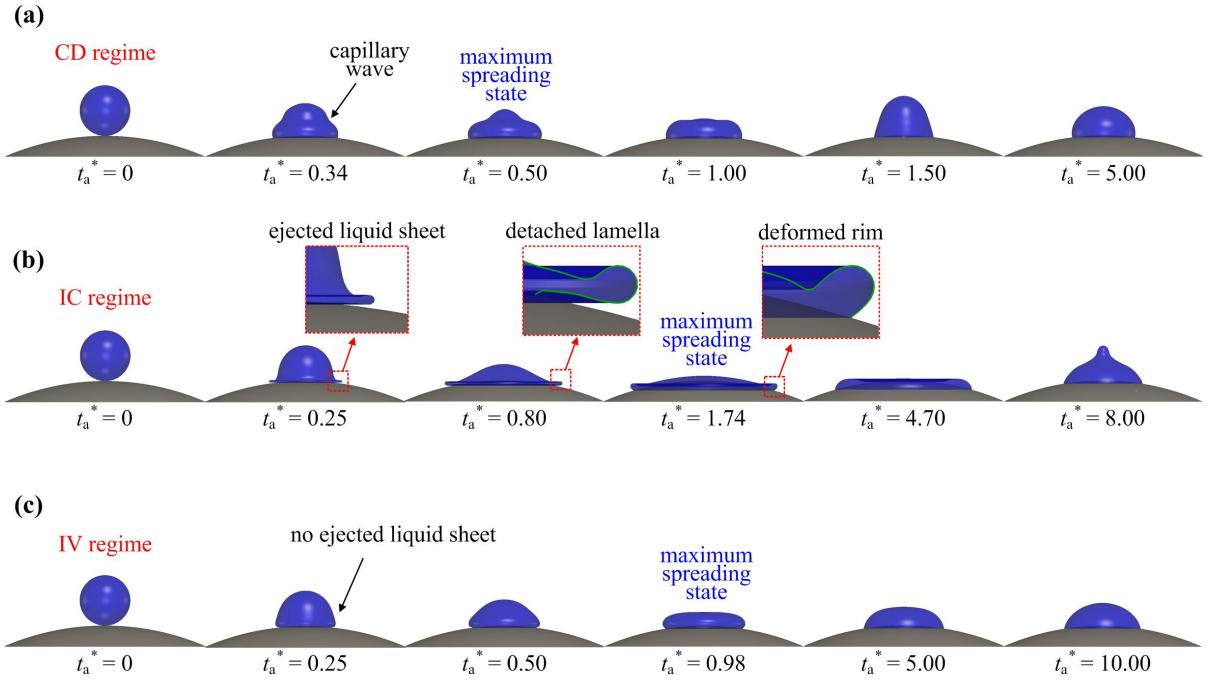

Fig. 3. Typical evolution of droplet interfacial morphology for the three different spreading regimes. (a) CD regime (We = 4, θ_{eqi} = 90° and Oh = 0.0026). (b) IC regime (We = 110, θ_{eqi} = 90° and Oh = 0.0026). (c) IV regime (We = 110, θ_{eqi} = 90° and Oh = 0.5246). In these cases, Ω = 1/10 for generality.

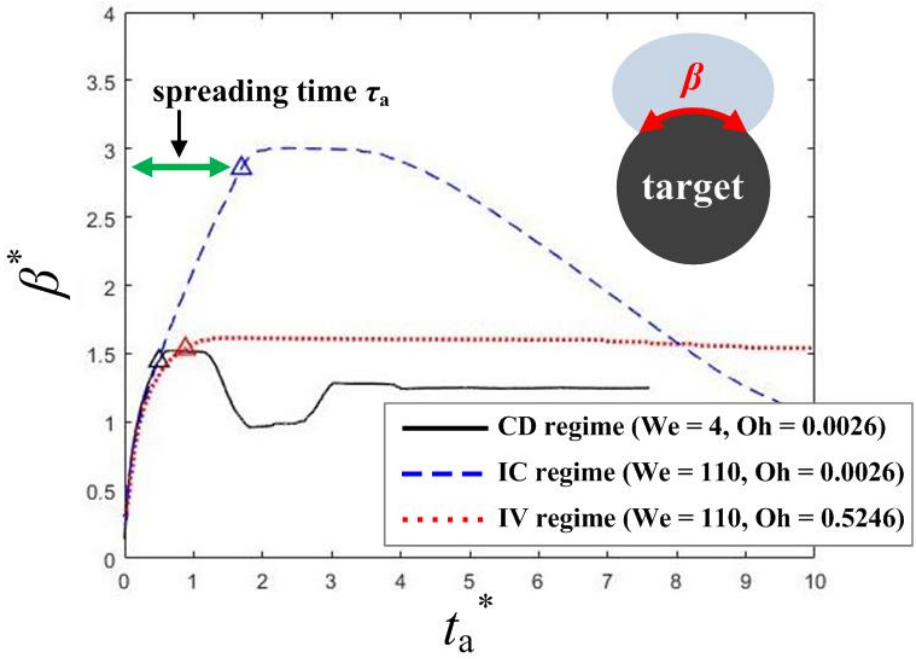

Fig. 4. Typical evolution of the non-dimensional spreading extent, β^*, for the three different spreading regimes. All collision conditions for each regime are the same as Fig.3. The inset depicts the schematic for measuring β^*. The spreading times (the time that a droplet attains 95 % of the maximum value of β^*) are also marked by the triangles.

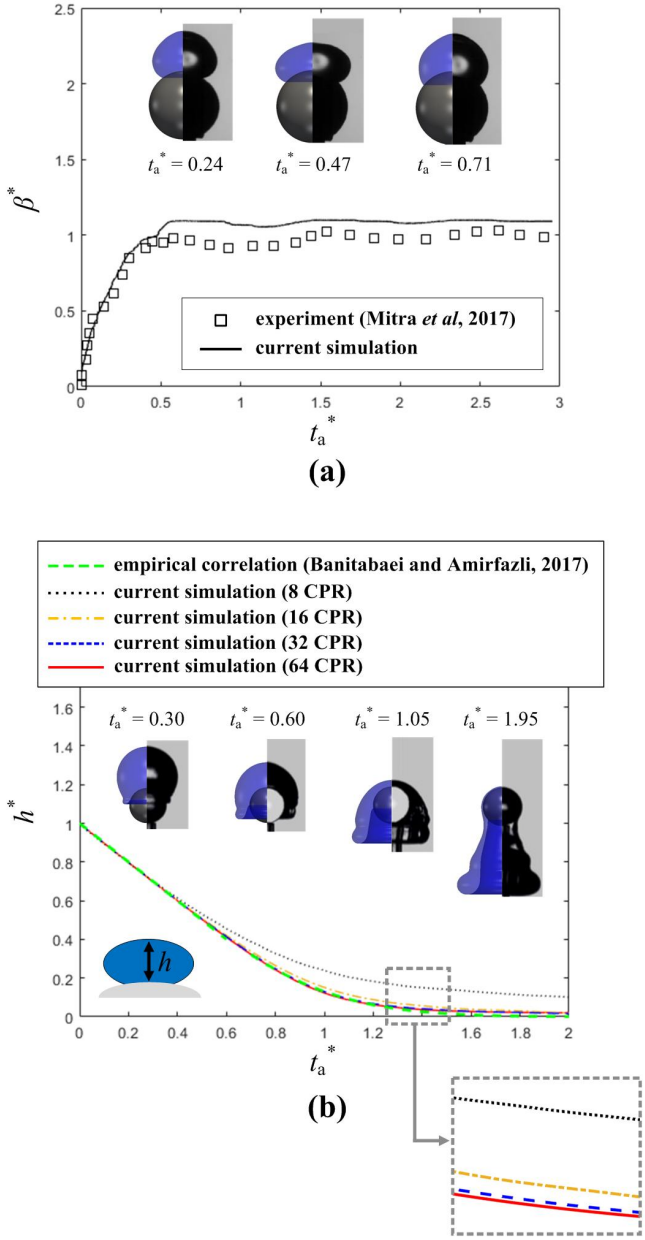

Fig. 5. Benchmark tests. (a) Evolution of the non-dimensional spreading extent, β^*, for a droplet spreading on a small spherical target at low We (We = 0.9, θ_{eqi} = 85°, Oh = 0.0026 and Ω = 0.83). The insets compare the interfacial shapes between the experiment [2] and the current simulation for 3 different time instants (t_a^* = 0.24, 0.47, and 0.71). Reproduced with permission from S. Mitra *et al*., "Interactions in droplet and particle system of near unity size ratio," Chem. Eng. Sci. **170**, 154–175 (2017). Copyright 2017 Elsevier, Ltd. (b) Evolution of the non-dimensional film thickness, h^*, for a droplet spreading on a small spherical target at high We (We = 155.5, θ_{eqi} = 97°, Oh = 0.0026 and Ω = 1.7) simulated by using 4 different grid resolutions (8, 16, 32 and 64 CPR). The insets compare the interfacial shapes between the experiment [71] and the current simulation for 4 different time instants (t_a^* = 0.30, 0.60, 1.05 and 1.95), whereas the other inset in the lower-left corner depicts the schematic for measuring h. Reproduced with permission from S. A. Banitabaei and A. Amirfazli, "Droplet impact onto a solid sphere: Effect of wettability and impact velocity," Phys. Fluids **29**, 062111 (2017). Copyright 2017 AIP Publishing LLC.

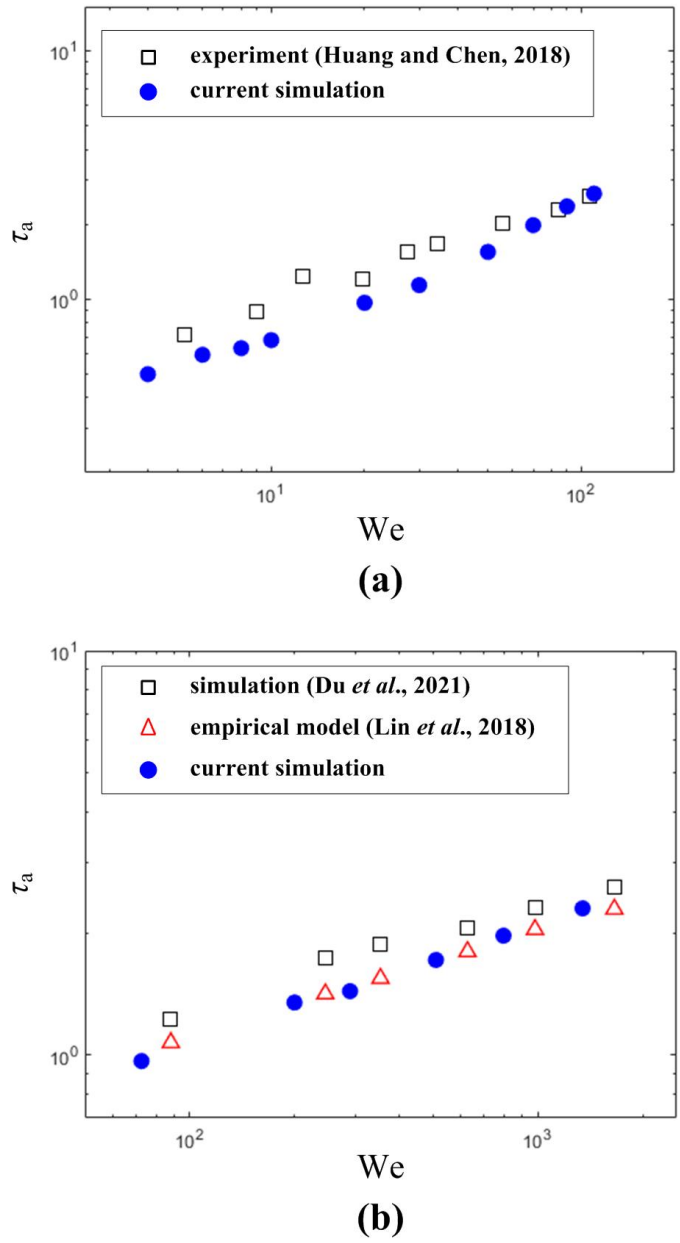

Fig. 6. Benchmark tests. (a) Non-dimensional advective spreading time, τ_a, at low Oh (Oh = 0.0026). The existing experimental result [18] is marked by black squares. (b) τ_a at high Oh (Oh = 0.62). The existing results from the numerical simulation [21] and the empirical correlation [19] are marked by black squares and red triangles, respectively.

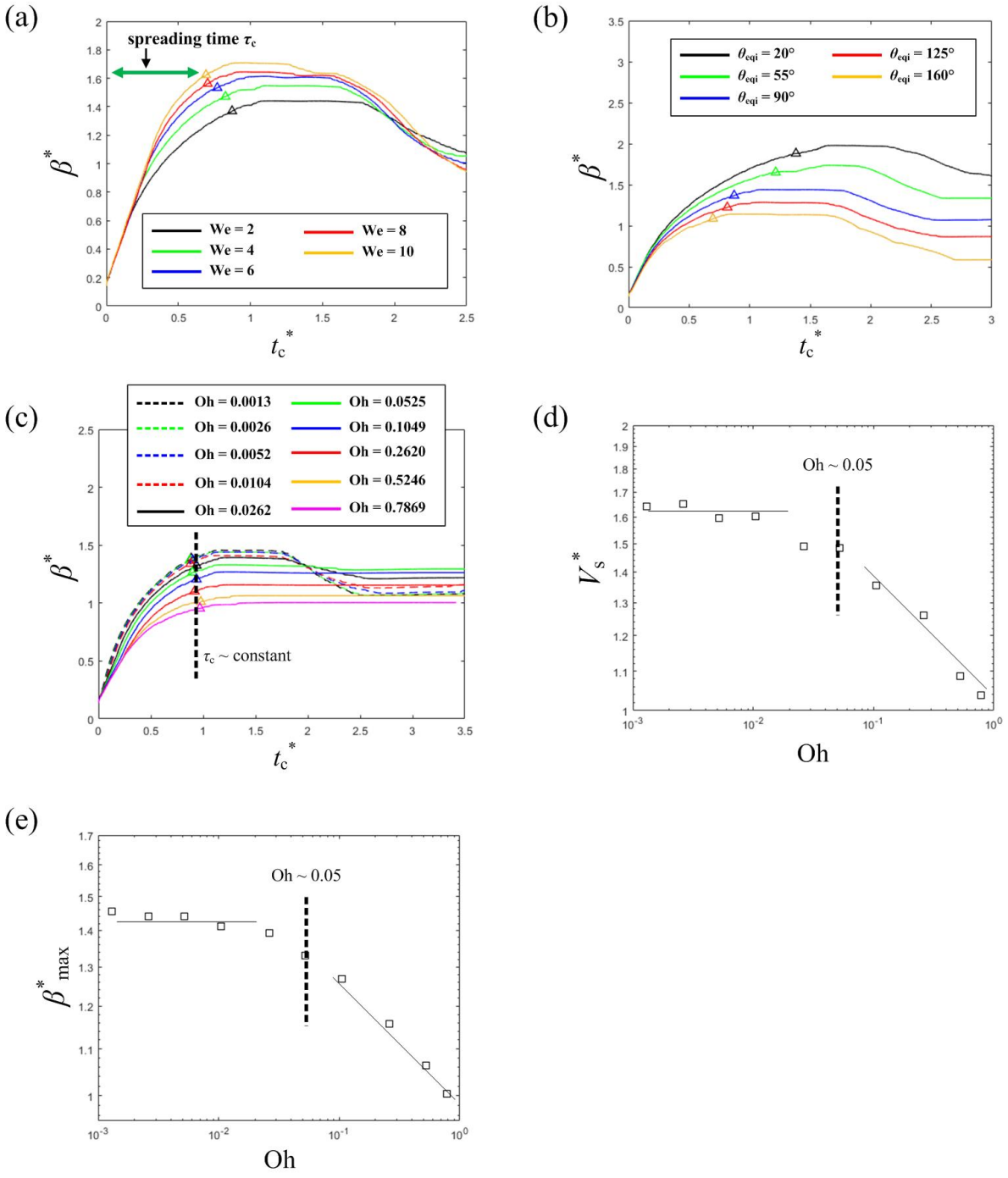

Fig. 7. Effect of the impact parameters on τ_c for the CD regime. (a) Effect of We (We = 2–10, θ_{eqi} = 90° and Oh = 0.0026). (b) Effect of θ_{eqi} (We = 2, θ_{eqi} = 20°–160° and Oh = 0.0026). (c) Effect of Oh (We = 2, θ_{eqi} = 90° and Oh = 0.0013–0.7869). (d) Effect of Oh on the non-dimensional spreading velocity, V_s^*. (e) Effect of Oh on the non-dimensional maximum spreading extent, β^*_{max}. For (d) and (e), all collision conditions are the same as Fig.7(c).

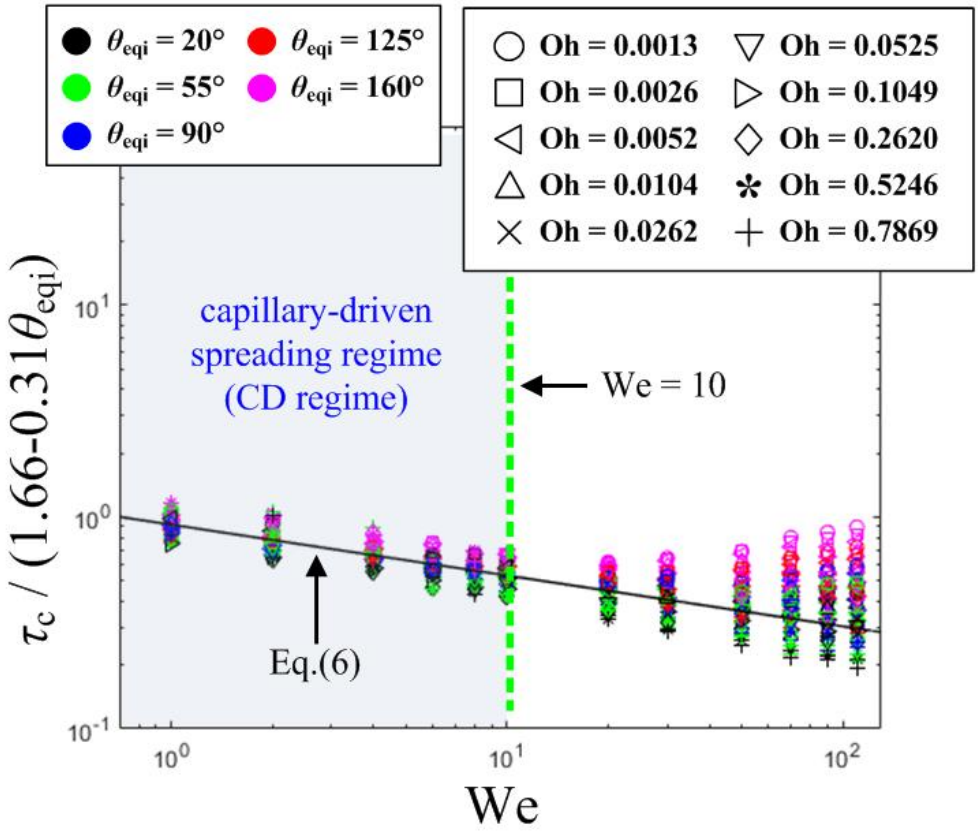

Fig. 8. A total of 600 τ_c data (We = 1–110, θ_{eqi} = 20°–160° and Oh = 0.0013–0.7869). The proposed prediction model, i.e., Eq.(6) for the CD regime is indicated by the black solid line. The green dashed line depicts the threshold for the CD regime.

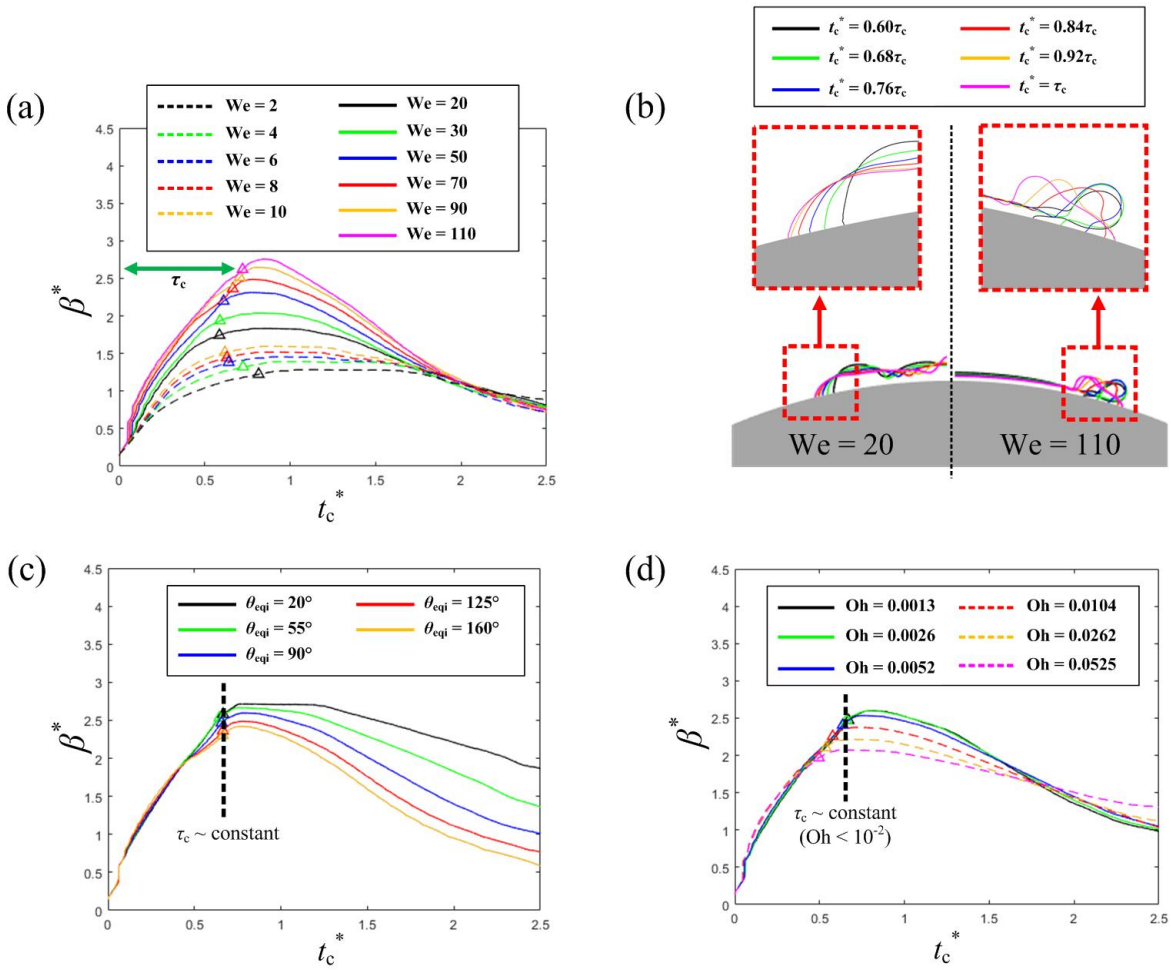

Fig. 9. Effect of the impact parameters on τ_c for the IC regime. (a) Effect of We (We = 20–110, θ_{eqi} = 125° and Oh = 0.0026). (b) Effect of We on the interfacial evolution of a droplet and its lamella deformation (We = 20 and 110, θ_{eqi} = 20° and Oh = 0.0026). (c) Effect of θ_{eqi} (We = 90, θ_{eqi} = 20°–160° and Oh = 0.0026). (d) Effect of Oh (We = 70, θ_{eqi} = 90° and Oh = 0.0013–0.0525).

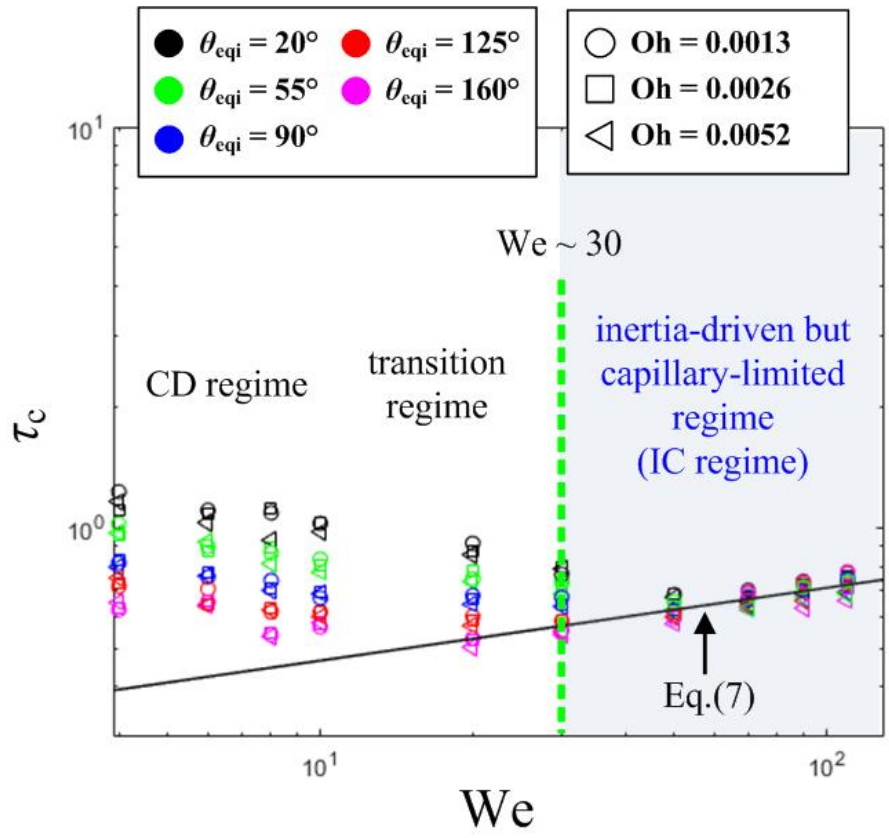

Fig. 10. A total of 150 τ_c data (We = 4–110, θ_{eqi} = 20°–160° and Oh = 0.0013–0.0052). The proposed prediction model, i.e., Eq.(7), for the IC regime is indicated by the black solid line. The green dashed line depicts the threshold for the IC regime.

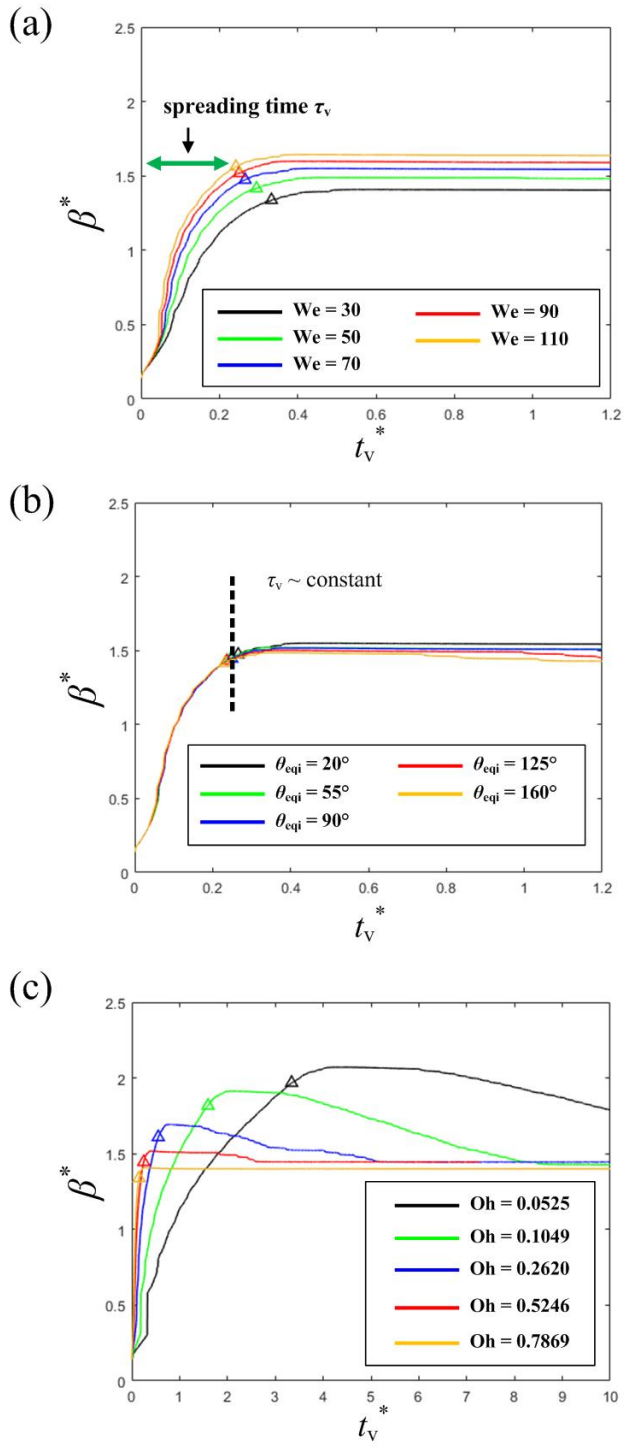

Fig. 11. Effect of the impact parameters on τ_v for the IV regime. (a) Effect of We (We = 30–110, θ_{eqi} = 20° and Oh = 0.5246). (c) Effect of θ_{eqi} (We = 70, θ_{eqi} = 20°–160° and Oh = 0.5246). (d) Effect of Oh (We = 70, θ_{eqi} = 90° and Oh = 0.0525–0.7869).

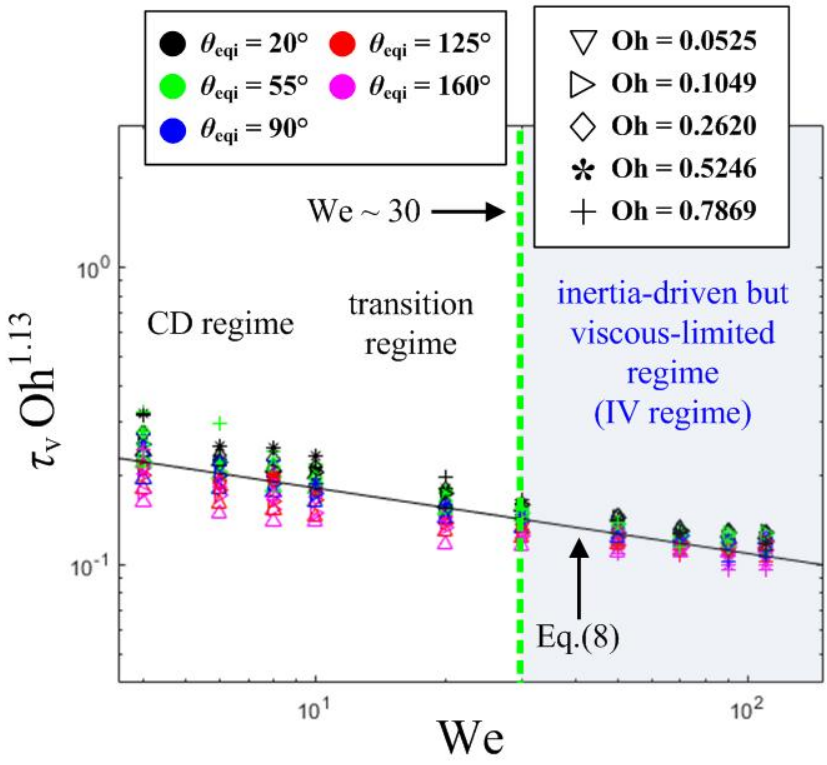

Fig. 12. A total of 250 τ_c data (We = 4–110, θ_{eqi} = 20°–160° and Oh = 0.0525–0.7869). The proposed prediction model, i.e., Eq.(8), for the IV regime is indicated by the black solid line. The green dashed line depicts the threshold for the IV regime.

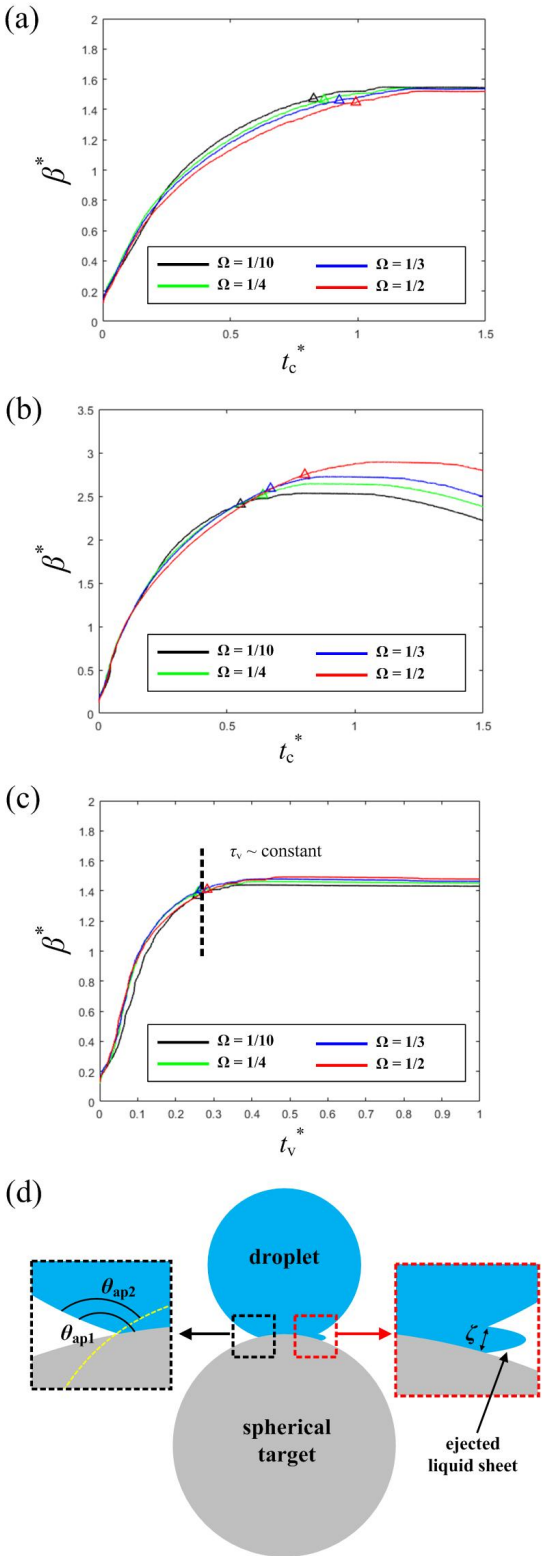

Fig. 13. (a) Effect of Ω on τ_c for the CD regime (We = 4, θ_{eqi} = 90°, and Oh = 0.0026). (b) Effect of Ω on τ_c for the IC regime (We = 50, θ_{eqi} = 90° and Oh = 0.0026). (c) Effect of Ω on τ_v for the IV regime (We = 50, θ_{eqi} = 90° and Oh = 0.5246). (d) Schematics of the initial apparent contact angles (on the left side) and the lamella characteristics (on the right side).

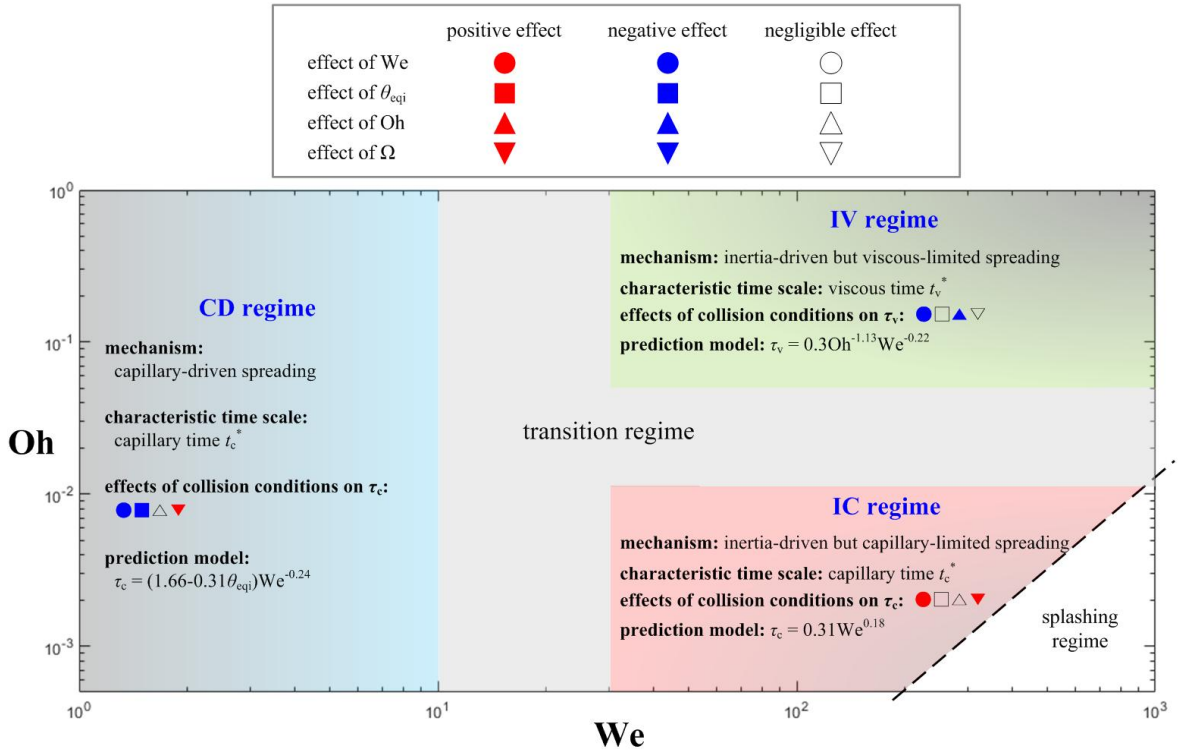

Fig. 14. Refined regime-map of the droplet spreading mechanism. Three different spreading regimes, i.e., CD, IC, and IV regimes with the transition area are depicted. The physical mechanism driving the spreading process, the characteristic time scale, the effects from 4 impact parameters (We, θ_{eqi}, Oh, and Ω) and the prediction models are also presented for each regime.

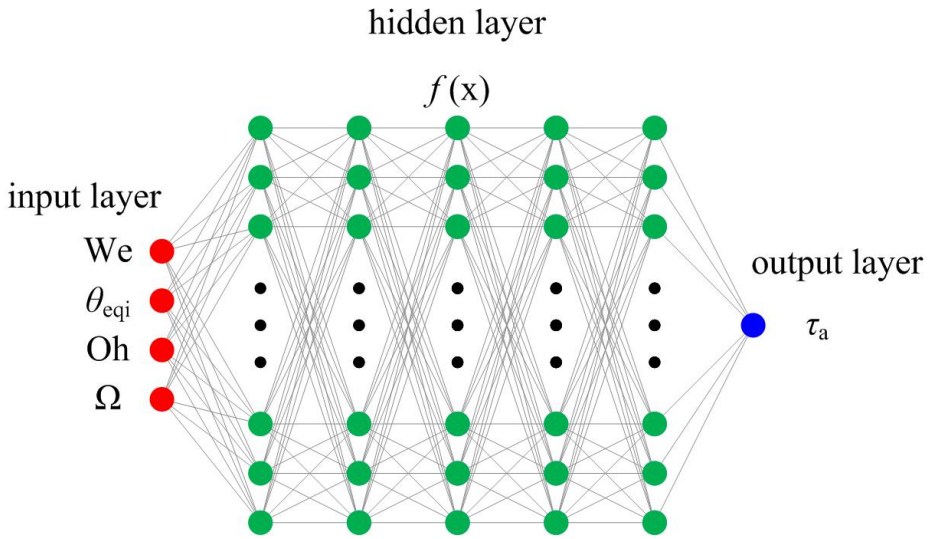

Fig. 15. Schematic diagram of the multilayer perceptron (MLP) used in the current study.

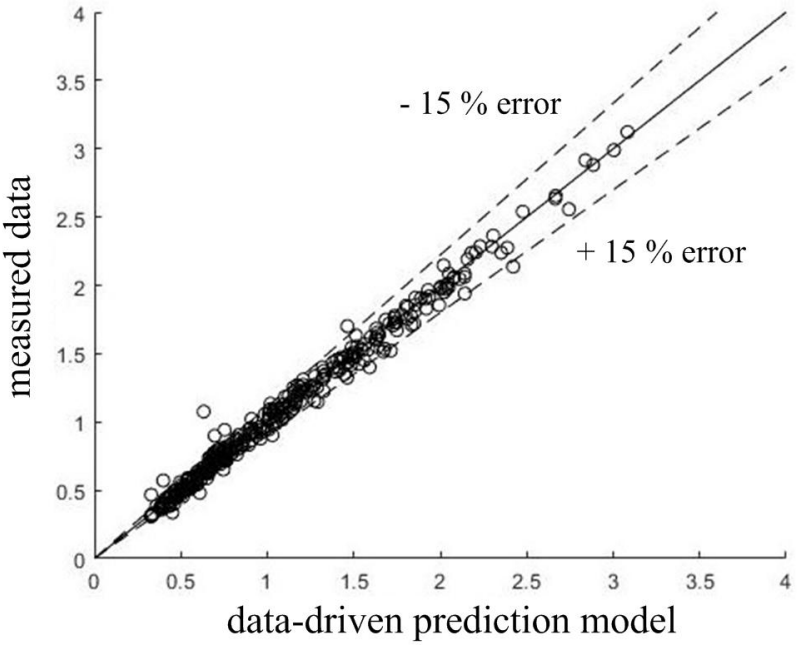

Fig. 16. Comparison of the spreading time, τ_a, between predicted data by using the data-driven (MLP) model and true (measured) data obtained by our simulations. The deviation range of ± 15% is marked by the two dashed-black lines.

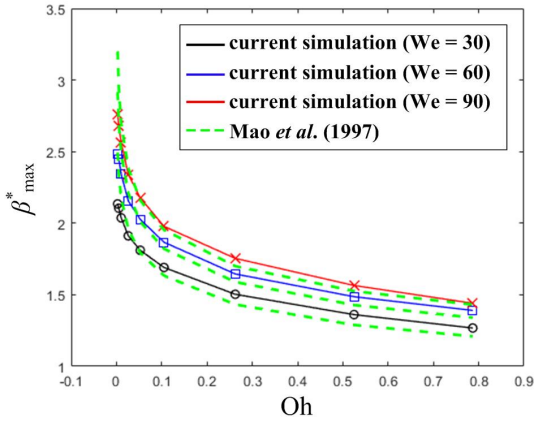

(a)

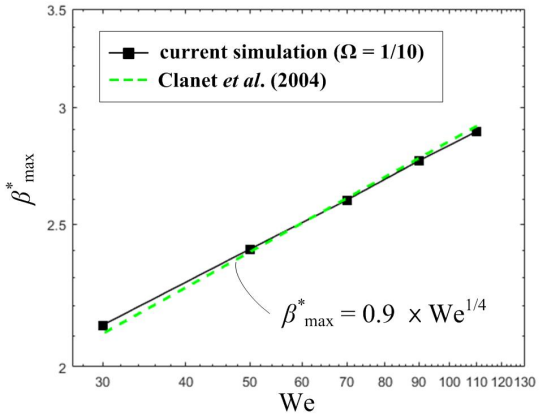

(b)

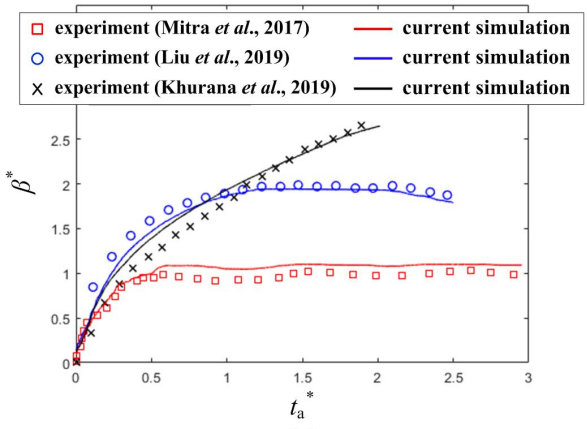

(c)

Fig. 17. Validation comparisons between our simulation results and existing experimental results. (a) Comparison with Mao *et al.*'s [25] semi-empirical model for droplet impact with a flat surface ($30 \leq We \leq 90$, $0.0013 \leq Oh \leq 0.7869$). (b) Comparison with Clanet *et al.*'s [16] empirical scaling law for droplet impact with a flat surface ($30 \leq We \leq 110$, $Oh = 0.0026$). (c) comparisons with the experimental data of Mitra *et al.* (red squares; $We = 0.9$, $\Omega = 0.83$, $\theta_{eqi} = 85°$, $Oh = 0.0024$) [2], Liu *et al.* (blue circles; $We = 19.2$, $\Omega = 0.15$, $\theta_{eqi} = 93°$, $Oh = 0.0022$) [38], and Khurana *et al.* (black crosses; $We = 35.3$, $\Omega = 0.60$, $\theta_{eqi} = 85°$, $Oh = 0.0022$) [39] for droplet impact with a spherical target. Reproduced with permission from I. Yoon and S. Shin [40], "Maximal spreading of droplet during collision on particle: effects of liquid viscosity and surface curvature," Phys. Fluids 33, 083310 (2021). Copyright 2021 AIP Publishing LLC.

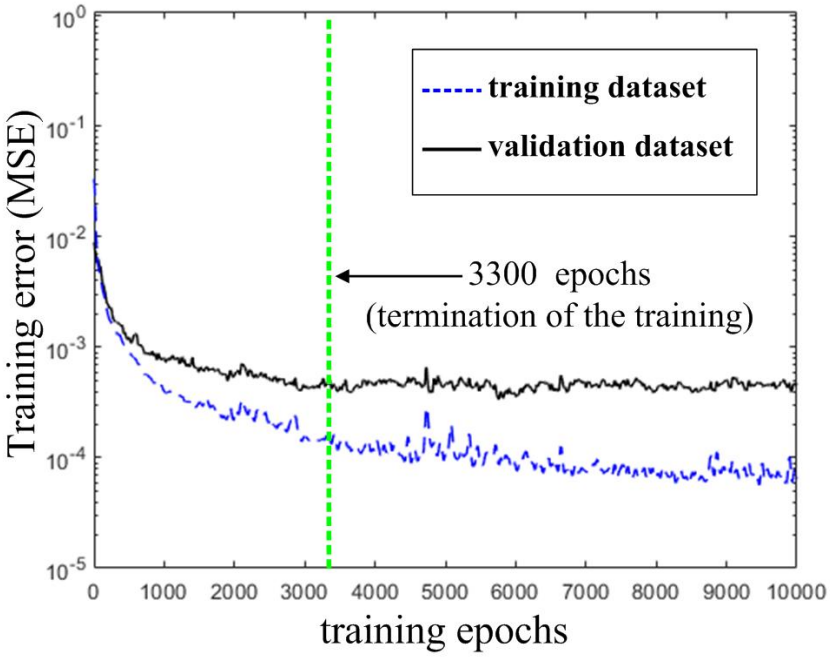

Fig. 18. Training errors (MSE) vs. training epochs for training and validation datasets. The training is terminated at 3300 training epochs where the MSE for the validation dataset (see black solid line) is sufficiently converged. The error for the validation dataset is 4.62×10^4.

GRAPHICAL ABSTRACT